

FEDERAL UNIVERSITY OF ABC  
NANOSCIENCE AND ADVANCED MATERIALS GRADUATE PROGRAM

Gustavo Mitsui Morishita

**DESENVOLVIMENTO DE ELETRODOS  
NANOESTRUTURADOS DE ÓXIDOS METÁLICOS PARA  
CONVERSÃO DE ENERGIA SOLAR EM ENERGIA  
QUÍMICA: COMBUSTÍVEL SOLAR**

**DEVELOPMENT OF NANOSTRUCTURED METAL OXIDE  
ELECTRODES FOR CONVERTING SOLAR ENERGY INTO  
CHEMICAL ENERGY: SOLAR FUEL**

Santo André, SP  
2023

GUSTAVO MITSUI MORISHITA

DESENVOLVIMENTO DE ELETRODOS NANOESTRUTURADOS DE ÓXIDOS  
METÁLICOS PARA CONVERSÃO DE ENERGIA SOLAR EM ENERGIA QUÍMICA:  
COMBUSTÍVEL SOLAR

DEVELOPMENT OF NANOSTRUCTURED METAL OXIDE ELECTRODES FOR  
CONVERTING SOLAR ENERGY INTO CHEMICAL ENERGY: SOLAR FUEL

Tese apresentada ao Programa de Pós-Graduação em Nanociências e Materiais Avançados da Universidade Federal do ABC como requisito parcial para obtenção do título de Doutor.

Thesis presented to the Nanoscience and Advanced Materials graduate program from Federal University of ABC in partial fulfillment of the requirements for obtain a PhD. degree.

Orientador/Advisor:

Prof. Dr. Flavio Leandro de Souza

Santo André, SP

2023

Sistema de Bibliotecas da Universidade Federal do ABC  
Elaborada pelo Sistema de Geração de Ficha Catalográfica da UFABC  
com os dados fornecidos pelo(a) autor(a).

Morishita, Gustavo Mitsui

Desenvolvimento de eletrodos nanoestruturados de óxidos metálicos para conversão de energia solar em energia química : combustível solar / Gustavo Mitsui Morishita. — 2023.

75 fls. : il.

Orientador: Flavio Leandro de Souza

Tese (Doutorado) — Universidade Federal do ABC, Programa de Pós-Graduação em Nanociências e Materiais Avançados, Santo André, 2023.

1. nanobastões de hematita. 2. conversão da energia solar. 3. dinâmica dos portadores de cargas. 4. dopagem. I. de Souza, Flavio Leandro. II. Programa de Pós-Graduação em Nanociências e Materiais Avançados, 2023. III. Título.

Este exemplar foi revisado e alterado em relação à versão original, de acordo com as observações levantadas pela banca no dia da defesa, sob responsabilidade única do autor e com a anuência de seu orientador.

Santo André, 15 de Fevereiro de 2023.

Assinatura do autor: Gustavo Mitsui Marishita

Assinatura do orientador: Flavio L Souza

Prof. Dr. Flavio Leandro de Souza  
Universidade Federal do ABC  
Lab. Energia Alternativa e Nanomateriais  
SIAPE 1760527



## MINISTÉRIO DA EDUCAÇÃO

### Fundação Universidade Federal do ABC

Avenida dos Estados, 5001 – Bairro Santa Terezinha – Santo André – SP  
CEP 09210-580 · Fone: (11) 4996-0017

#### FOLHA DE ASSINATURAS

Assinaturas dos membros da Banca Examinadora que avaliou e aprovou a Defesa de Tese de Doutorado do candidato, GUSTAVO MITSUI MORISHITA realizada em 12 de Dezembro de 2022:

Prof.(a) **DERECK NILLS FERREIRA MUCHE**  
UNIVERSIDADE FEDERAL DE SÃO CARLOS

Prof.(a) **GUSTAVO MARTINI DALPIAN**  
UNIVERSIDADE FEDERAL DO ABC

Prof.(a) **JOAO BATISTA SOUZA JUNIOR**  
LABORATÓRIO NACIONAL DE NANOTECNOLOGIA

Prof.(a) **MARCOS DE ABREU AVILA**  
UNIVERSIDADE FEDERAL DO ABC

Prof.(a) **MURILO SANTHIAGO**  
CENTRO NACIONAL DE PESQUISA EM ENERGIA E MATERIAIS

Prof.(a) **SYDNEY FERREIRA SANTOS**  
UNIVERSIDADE FEDERAL DO ABC

Prof.(a) **WENDEL ANDRADE ALVES**  
UNIVERSIDADE FEDERAL DO ABC

Prof.(a) **FLAVIO LEANDRO DE SOUZA**  
UNIVERSIDADE FEDERAL DO ABC - Presidente

\* Por ausência do membro titular, foi substituído pelo membro suplente descrito acima: nome completo, instituição e assinatura

## **DEDICATION**

I dedicate this work to my parents Edson and Sueli who have always supported and encouraged me in my studies, to my sisters Danyelle and Suellen for all their support, and to my niece Sophia, who I wish she always seeks the path of studies as a priority in life.

## **ACKNOWLEDGMENT**

I thank my advisor Prof. Dr. Flavio Leandro de Souza for all the support provided, for mentoring, for patience, and for the opportunity to be part of his research group. A special thanks to my friends and laboratory colleagues: Lizandra, Gabriel, Ingrid, and Karen.

I would like to thank the support from Brazilian National Nanotechnology Laboratory (LNNANO), and the Brazilian Center for Research in Energy and Materials (CNPEM). I am grateful to the LNNANO's staff: Najara, Otávio, Carlos, Cleyton, Fabiano, João Marcos, Elcio, Fabio Zambello, Carol, and Bruna.

I would like to thank the support from Brazilian National Nanotechnology Laboratory (LNNANO), Brazilian Center for Research in Energy and Materials (CNPEM), and Coordenação de Aperfeiçoamento de Pessoal de Nível Superior (CAPES). A special thank for the founding to Conselho Nacional de Desenvolvimento Científico e Tecnológico (CNPQ) by process grant number 161885/2019-5. A special thanks to SHELL and Fundação de Amparo à Pesquisa do Estado de São Paulo (FAPESP) to provide the scholarship and founding for this work by process grant number 17/11986-5.

This study was financed in part by the Coordenação de Aperfeiçoamento de Pessoal de Nível Superior - Brazil (CAPES) - Finance Code 001

## RESUMO

A grande pegada de carbono e as consequências devastadoras das mudanças climáticas geradas pela extração, produção e utilização de combustíveis fósseis exigem a transição para recursos de energia limpa e sustentável para atender à demanda global de energia, respeitando a saúde humana e o meio ambiente. Devido à sustentabilidade e versatilidade ambiental, o hidrogênio verde (gerado a partir de fontes de energia renováveis) foi legitimamente promovido como o combustível do futuro na transição para sociedades de zero carbono. A produção de hidrogênio a partir da luz solar e da quebra da molécula da água oferece uma oportunidade única de se utilizar os dois recursos naturais gratuitos mais abundantes e geograficamente equilibrados disponíveis, ou seja, utilizar o sol e a água do mar para gerar energia limpa verdadeiramente sustentável e ecológica. A hematita ( $\alpha\text{-Fe}_2\text{O}_3$ ) é um material promissor para alcançar uma alta eficiência solar para hidrogênio devido ao seu *bandgap* favorável, estabilidade, custo-benefício e abundância de terra. No entanto, as desvantagens da hematita, como a baixa mobilidade dos portadores de carga e a altas taxas de recombinação do par elétron-buraco, inibiram seu desempenho, que é notoriamente inferior ao valor teórico. Esta tese visa melhorar o desempenho da hematita durante o processo da separação da água com o uso da luz solar, otimizando os processos de cinética de portadores diretamente relacionados às interfaces sólido-sólido e sólido-líquido. Uma introdução à nossa área de pesquisa é dada no Capítulo 1, seguida por uma descrição dos objetivos, originalidade e metodologia utilizadas nesse trabalho são mostradas nos Capítulos 2-4.

O Capítulo 5 está dividido em cinco seções diferentes; a primeira parte concentra-se na determinação da temperatura ideal para a síntese em condição hidrotermal. A segunda seção é dedicada principalmente a estabelecer o efeito da inserção de elementos modificantes sobre a hematita. Em seguida, mostramos o estudo de uma modificação entre a camada condutora transparente (TCO) e o foto ânodo. As estratégias simultâneas trouxeram um aumento da fotocorrente três vezes em comparação com o eletrodo de Hematita puro. Para a hematita modificada com háfnio (Hf) depositada em uma camada de  $\text{ZrO}_2$ , foi observado uma redução a perda de elétrons após ser coletado pelo FTO. Embora estudos experimentais demonstrem que o Hf não está inserido na rede cristalina da hematita, ele induz uma redução do diâmetro dos nanobastões de  $32\pm 2$  para  $26\pm 2$  nm, com consequente aumento da área de superfície ativa. As medidas de voltametria de varredura linear com iluminação de  $100 \text{ mW cm}^{-2}$  em uma espessura de fotoânodo de 500 nm mostraram uma densidade de fotocorrente de  $2,07 \text{ mA cm}^{-2}$  a 1,23 V em um eletrodo reversível de hidrogênio (RHE). O valor contrasta com a hematita pura ( $0,75$



mA cm<sup>-2</sup>), destacando-se o papel do desenvolvimento de fotoânodos para o aumento da eficiência da produção de hidrogênio verde via energia solar.

Palavras-chave: nanobastões de hematita, conversão da energia solar, dinâmica dos portadores de cargas, dopagem.

## ABSTRACT

The vast carbon footprint and climate change shattering consequences generated by fossil fuels extraction, production, and utilization mandate the transition to clean and sustainable energy resources to fulfill global energy demand while respecting human health and the environment. Due to environmental sustainability and versatility, *green* hydrogen (generated from renewable energy sources) has been rightfully pushed as the fuel of the future for transitioning to carbon-zero/net-zero societies. Solar water-splitting hydrogen production provides a unique opportunity to use the two most abundant and geographically balanced free natural resources available, i.e. the sun and seawater to generate truly sustainable and environment-friendly clean energy. Hematite ( $\alpha\text{-Fe}_2\text{O}_3$ ) is a promising material to achieve a high solar to hydrogen efficiency due to its band gap energy, stability, cost-effectiveness, and earth abundance. However, hematite drawbacks such as low carrier mobility and fast electron-hole recombination rates inhibited its performance which is notoriously lower than the theoretically value. This thesis aims to improve the hematite performance during solar water splitting, by optimizing the carrier kinetics processes directly related to the solid-solid and solid liquid interfaces. An introduction to the field is given in *Chapter 1* followed by a description of the objectives, originality and experimental methods used herein in *Chapter 2-4*.

*Chapter 5* is divided into five different sections; the first part is focused on determining the optimal temperature for hydrothermal synthesis. The second section is mainly dedicated to establishing the effect of element insertion on the hematite layer. Then, the impact of a modification between the transparent conductive substrate (TCO) and the photoabsorber is also shown in this section. The simultaneous strategies brought a three-fold photocurrent increase compared to the bare electrode. For Hafnium (Hf) -modified hematite deposited onto a  $\text{ZrO}_2$  layer, a reduced electron loss from the back-injection into the FTO contact support is quantified. Although experimental studies demonstrate that Hf is not inserted in the hematite network, it induces a nanorod diameter reduction from  $32\pm 2$  and  $26\pm 2$  nm, with a consequent increase in the active surface area. The linear sweep voltammetry measurements with  $100\text{ mW cm}^{-2}$  illumination in a 500 nm photoanode thickness showed a photocurrent density of  $2.07\text{ mA cm}^{-2}$  at 1.23 V in a reversible hydrogen electrode (RHE). The value contrasts with the bare hematite rods ( $0.75\text{ mA cm}^{-2}$ ), highlighting the photoanode design's role in improving solar power hydrogen production.

Keyword: hematite nanorods, solar energy conversion, charge carrier dynamics, doping.

## LIST OF IMAGES

Figure 1 - Scheme of a photoelectrochemical cell, composed of an n-type photoanode and a cathode immersed in an alkaline electrolyte. The OER and HER are shown for each process, according to the bandgap for solar to hydrogen conversion. ....	19
Figure 2 - Scheme of photoanode and where the parameters of equation (2.6) impact. ....	23
Figure 3- $J_{ph}$ of an ideal hematite photoanode (solid black line), a $J_{ph}$ obtained experimentally (solid grey line), an improvement of $\eta_{sep}$ (dashed black line), and an improvement of $\eta_{cat}$ (dotted grey line). Adapted with permission from Sivula et al., ChemSusChem 4, 432–449 (2011). Copyright 2011 WILEY-VCH Verlag GmbH & Co. ....	23
Figure 4 - Scheme of the strategies of doped hematite according to the location of element doping. Published in: Joao B. Souza Junior; Flavio L. Souza; Lionel Vayssieres; Oomman K. Varghese; Appl. Phys. Lett. 119, 200501 (2021). Copyright © 2021 Author(s) ....	25
Figure 5 - Scheme of the hydrothermal process, from left to the right side we start with the allocation of the precursor solution and the substrate in the Teflon vessel and insert them in the autoclave. Afterward, we have the film growth under hydrothermal conditions following the ice bath, in which first we obtain the $\beta$ -FeOOH phase and after the heat treatment the hematite phase.....	31
Figure 6 - Scheme of modifier addition. Onto the film in the $\beta$ -FeOOH phase, we deposited 50 $\mu$ L of the modifier solution via spin coating, and then the same process followed as previously said. ....	32
Figure 7 - Scheme of blocking layer design. Onto an already cleaned substrate, we deposited 50 $\mu$ L of the solution of the element via spin coating, this procedure is repeated twice, and then the substrate coated is subjected to thermal treatment and cooling down to room temperature ( $\sim 296$ K) naturally. ....	33
Figure 8 - a, b, and c shows the as-prepared $\beta$ -FeOOH obtained after hydrothermal synthesis at 373, 393, and 413 K respectively. d, e, and f show the photoelectrode after thermal treatment. ....	36
Figure 9- Spectrophotometry spectrum of the fluorine-doped tin oxide (FTO) glass substrate, and of samples for the Akaganéite phase (dash lines) and Hematite phase (solid lines).....	37
Figure 10 - Linear Sweep Voltammetry curves under light, calibrated at $100 \text{ mW cm}^{-2}$ , and dark conditions in NaOH (1.0 M) aqueous solution.....	38
Figure 11 - X-ray diffraction of the sample synthesized under hydrothermal conditions at 393K for 2h followed by a thermal treatment in an $N_2$ atmosphere.....	38

Figure 12 – a) AFM measurement and the respective roughness of hematite thin films synthesized under hydrothermal conditions at 393K for 2h followed by a thermal treatment in an N <sub>2</sub> atmosphere. b) FIB-SEM image of the cross-section view, and c SEM image of the top view.....	39
Figure 13 - Spectrophotometry of Hem, HHf, HTa, and HZr.....	40
Figure 14 - Linear Sweep Voltammetry analysis of H, HHf, HTa, and HZr under light calibrated at 100 mW cm <sup>-2</sup> and dark conditions in NaOH (1.0 M) aqueous solution.....	41
Figure 15 - Spectrophotometry and linear sweep voltammetry data of the triplicate for: a Hem, b HHf, c HTa, and d HZr. ....	41
Figure 16 – Linear sweep voltammetry analysis for spin coating optimization for Hf <sup>4+</sup> addition under light calibrated at 100 mW cm <sup>-2</sup> and dark conditions in NaOH (1.0 M) aqueous solution. ....	42
Figure 17 – Linear sweep voltammetry analysis for spin coating optimization for Ta <sup>5+</sup> addition under light calibrated at 100 mW cm <sup>-2</sup> and dark conditions in NaOH (1.0 M) aqueous solution. ....	43
Figure 18 – Linear sweep voltammetry analysis for spin coating optimization for Zr <sup>4+</sup> addition. ....	44
Figure 19 - Study of photoelectrodeposition cocatalyst on the pristine hematite and hematite-modified films. The LSV was measured under light calibrated at 100 mW cm <sup>-2</sup> and dark conditions in NaOH (1.0 M) aqueous solution.....	45
Figure 20 – Mott-Schottky analysis in darkness at 1kHz for Hem, HHf, HTa, and HZr samples. ....	46
Figure 21 - Flatband potential determination for a) Hem, b) HHf, c) HTa, and d) HZr.....	47
Figure 22 - X-ray diffraction patterns for Hem, HHf, HTa, and HZr.....	48
Figure 23 - UV-Vis measurement of the FTO with and without the blocking layer coating. On the left side, we show the UV-Vis spectra of bare FTO, and on the right side the UV-Vis spectra of the FTO covered with the blocking layer, showing that the blocking layer does not improve the light absorption. ....	49
Figure 24 - Blocking layer study with the elements: Al <sub>2</sub> O <sub>3</sub> , HfO <sub>2</sub> , Nb <sub>2</sub> O <sub>5</sub> , Ta <sub>2</sub> O <sub>5</sub> , TiO <sub>2</sub> , and ZrO <sub>2</sub> .....	50
Figure 25 - Cyclic voltammetry (CV) of blocking layer optimization. CV measurements were recorded from 0.7 to 1.6 VRHE, using a scan rate of 10 mV s <sup>-1</sup> immersed in Aan electrolyte solution containing 1.0 M of KOH, and 10 mM of K <sub>4</sub> [Fe(CN) <sub>6</sub> ].....	51

Figure 26 - Linear sweep voltammetry of different conditions of the blocking layer design. The LSV curves were measured under light calibrated at $100 \text{ mW cm}^{-2}$ and dark conditions in NaOH (1.0 M) as electrolyte solution. ....	52
Figure 27 - X-ray diffraction of H, HHf, and Zr/HHf samples. ....	53
Figure 28 - a, b, and c is the topographic image obtained from Atomic Force Microscopy of the Hem, HHf, and Zr/HHf, respectively. a", b", and c" are FIB-SEM images of the cross-section view of the Hem, HHf, and Zr/HHf, respectively. a"', b"', and c"' are FIB-SEM images of the top view of the Hem, HHf, and Zr/HHf, respectively. ....	54
Figure 29 - Energy-dispersive X-ray spectroscopy analysis of Zr/HHf. ....	55
Figure 30 - Spectrophotometry analysis of H, HHf, and Zr/HHf. ....	55
Figure 31 - Compilation of the photocurrent curves of the investigated samples. The LSV were measured under light calibrated at $100 \text{ mW cm}^{-2}$ and dark conditions in NaOH (1.0 M) as electrolyte solution. ....	56
Figure 32 - Mott-Schottky plot of H, HHf, and Zr/HHf samples. ....	57
Figure 33 - Nyquist plot from IMPS analysis of Hem. ....	59
Figure 34 - Nyquist plot from IMPS analysis of HHf. ....	59
Figure 35 - Nyquist plot from IMPS analysis of Zr/HHf. ....	60
Figure 36 - Transfer and RC constants in the function of applied potentials. ....	60
Figure 37 - Recombination and RC constants in the function of applied potentials. ....	61
Figure 38 - Charge separation efficiency versus applied potential. ....	61

# CONTENT

1. INTRODUCTION .....	15
1.1. Green hydrogen .....	16
1.2. Semiconductors .....	17
1.3. Photoelectrochemical cell .....	18
1.4. Iron Oxide .....	21
1.5. Hematite modifications .....	24
1.5.1. Modifier: Antimony on Hematite .....	26
1.5.2. Modifier: Zirconium oxide (ZrO <sub>2</sub> ) on hematite .....	27
1.5.3. Modifier: Hafnium on hematite .....	27
1.6. Mitigation of the electron loss at fluorine-doped-tin oxide/photoelectrode interface	28
2. ORIGINALITY AND CHALLENGES OF THE PROJECT .....	29
3. OBJECTIVES .....	30
4. EXPERIMENTAL SECTION .....	31
4.1. Synthesis of photoelectrodes .....	31
4.1.1. Substrate properties and cleaning process .....	31
4.1.2. $\alpha$ -Fe <sub>2</sub> O <sub>3</sub> Synthesis procedure .....	31
4.1.3. Modifiers addition .....	32
4.1.4. Blocking layer coating .....	32
4.2. Optical properties .....	33
4.3. Photoelectrochemical characterization .....	33
4.4. Structural and morphological characterization .....	34
4.5. Photoelectrodeposition of cocatalyst .....	35
5. RESULTS .....	36
5.1. Hematite .....	36
5.2. Hematite modification .....	39

5.2.1. Element addition.....	39
5.3. Blocking layer .....	48
5.4. Photoelectrodes study .....	52
5.5. Charge carrier dynamic.....	57
6. CONCLUSION.....	62
7. REFERENCES .....	63

## 1. INTRODUCTION

The hydrogen economy emerges, in a social context[1], as an attractive solution to global challenges and environmental crises [2]–[8]. In terms of the actual energy system, the energy worldwide system is provided 80% by fossil fuels [2], [3], [5]–[8]. The fossil fuel combustion process release gases that cause the greenhouse effect, which has been accumulating in high concentration in the atmosphere, attacking the environment and impacting the earth's climate [2]–[5], [7]–[11]. To decrease global greenhouse gas emissions, governments must implement a global-energy revolution as soon as possible (due to the increasing population, which increases the energy demand) [3]–[7]. In December 2015, almost 200 countries signed the Paris Agreement to control greenhouse gas emissions to keep global warming at or below 1.5 °C, which was ratified during the Conference of the Parties (COP26). As part of this agreement, the International Energy Agency (IEA) committed to leading a clean energy transition toward a sustainable future, with the goal of net-zero emissions by 2050.

Hydrogen represents an ideal option as a chemical fuel since it can be generated directly via clean, sustainable, and renewable processes [2], [3], [6], [10]–[12], releasing only water as a combustion by-product [4]. The hydrogen economy is seen as a key transition to a low-carbon future since it is capable of meeting the energy demands in several economic sectors without releasing any CO<sub>2</sub> or other pollutants [13], [14].

Hydrogen has been already used in the industry for petroleum refinement [6], [9], [10], [12], ammonia production for fertilizers, food processes, semiconductors, glass, and steel industries [9]. As a fuel, the National Aeronautics and Space Administration (NASA), from United State, European, and Japanese space programs, use hydrogen and oxygen liquid in the onboard fuel cells of the space shuttles, which is responsible to deliver energy and water to the astronauts[9]. In terms of electricity generation, wind power generates electricity on the island of Utsira in the Atlantic Ocean and the oversupply is used to produce hydrogen from electrolysis, which is storage to be employed in a fuel cell when the wind electricity is not enough [10]. Another form to generate electricity from Hydrogen is using photovoltaic (PV) cells to convert the sunlight into Hydrogen and Oxygen gas by water electrolysis[3], [8]–[10], [12], which are combusted and converting the mechanical movement into electricity [9], [10], [12].



### 1.1. Green hydrogen

Hydrogen can be classified depending on the sustainability of this energy vector, which is principally related to the production technology and the energy source. There is no universal standard name or classification, and it can change according to the country and even to the definition [15]. Recently, Lubbe et. al. 2022 [15], listed 12 hydrogen color classifications, and also propose a new color called golden. The most common hydrogen classification is gray, blue, or green. The term gray hydrogen refers to the generation of hydrogen from fossil fuels, such as natural gas. Gray hydrogen represents 95% of the commercial hydrogen produced, primarily from steam methane reforming at temperatures close to 1273 K. This endothermic reaction ( $\text{CH}_4 + \text{H}_2\text{O} \leftrightarrow 3\text{H}_2 + \text{CO}$ ) involves an exothermic water–gas shift reaction ( $\text{CO} + \text{H}_2\text{O} \leftrightarrow \text{H}_2 + \text{CO}_2$ ) during the process [16], [17]. Consequently, natural gas is converted into a mixture of hydrogen,  $\text{CO}_2$ , and impurities such as CO and unconverted  $\text{CH}_4$ , which requires an additional purification step to separate the desired gas [18]. Nevertheless, even the highly efficient steam methane reforming process releases 8.1 tons of  $\text{CO}_2$  per ton of hydrogen produced [19]. From an environmental perspective, it is unacceptable to produce a “clean” energy carrier that emits substantial amounts of greenhouse gases. However, from an economic standpoint, gray hydrogen is currently more advantageous than other types of hydrogen in terms of cost-benefit ( $\sim \$2.0 \text{ kg}^{-1}$ ) [20].

An alternative for reducing the environmental impact caused by gray hydrogen production uses technologies for carbon capture and storage during the steam methane reforming process and coal gasification, resulting in so-called blue hydrogen [21]. The present infrastructure and compatibility of blue hydrogen represent an attractive method for hydrogen production. However, the use of blue hydrogen remains low due to the sluggish development of large-scale carbon capture and storage plants [22].

Green hydrogen, which is produced from renewable energy sources such as solar or wind, has been praised as the clean energy source for the future because it produces no carbon emissions. Efforts have been made to produce green hydrogen using various methods according to their feasibility, environmental impact, and the availability of renewable sources [13], [20], [23]–[29].

It is important to know that Hydrogen is not a primary energy source [2]. Furthermore, some devices can be used to promote solar water splitting: photovoltaic devices, photocatalytic cells, and photoelectrochemical (PEC) cells [30]. Aiming for clean and renewable hydrogen, the process using PEC devices has been demonstrated to be very promising since its prototype

was proposed by Fujishima & Honda (1972) [31] where the authors showed that  $\text{TiO}_2$  semiconductor films can promote water splitting when illuminated [31]. Based on that principle, the research community has been trying to obtain an ideal material, low-cost, and scalable production process.

The following sections will discuss some fundamental concepts that provide an understanding of the developed work.

## 1.2. Semiconductors

The following properties that will be discussed are based on materials that can be classified into three classes: conductors, semiconductors, and insulators [32]. The energy band model provides an essential explanation of the optical and electronic properties of these types of material. The theory argues that in solid states an overlap of several molecular orbitals leads to the formation of a band of orbitals with similar energy, where the highest energy band occupied with electrons (at 0 K) is the valence band (VB) and the lower energy band unoccupied is the conduction band (CB) [32]. The energy difference between the valence band and the conduction band is called the band gap (BG).

The current flow is generated with the transport of the charge carrier throughout the material. A system with a large band gap ( $> 4.0$  eV) [33] that prevents the promotion of the charge carrier from the VB to CB is classified as an insulator. In counterpart, a system with easily charged carrier motion is a conductor, e.g., metals. When heated, the conductivity of metal decrease due to the increase of atoms' vibration. Semiconductors are insulators when the system is under equilibrium (at 0K), however when the temperature increases or under externally applied potential the conductivity increases. This is possible due to the band gap of semiconductors being around 2eV, where the negative charge carrier (electron) can be easily excited to the conduction band, and consequently, a positive carrier (hole) is left in the valence band. However, the amount of the charge carrier excited from VB to CB does not mean that the current flow will increase or even will have a current, this will depend on the capability of the material to transport the charge carrier.

Semiconductor materials are classified as intrinsic semiconductors when the material has not included any significant doping agents in their structure or when the elemental doping modifies the amount and also equilibrates the charge carrier,  $n = p$ , which is due to the creation of the electron and hole is in pairs. Extrinsic semiconductors are classified when impurities are incorporated into the structure to enhance the electrical properties, which means enhancing the

charge carrier ( $n \neq p$ ). An extrinsic semiconductor can be classified according to the amount of charge carrier in the valence and conduction band, where if the majority carrier is negative and the minority carrier is positive, is an n-type semiconductor, and if the majority carrier is positive and the minority carrier is negative, is classified as a p-type semiconductor [34].

The optical properties of semiconductors bring essential information about light absorption since the BG can be determined. The coefficient absorption ( $\alpha$ ) is given by the following equation (Eq. (1)):

$$\alpha = \frac{A (h\nu - BG)^m}{h\nu} \quad (1)$$

where A is a constant and m depends on the nature of the optical transitions, where  $m = 1/2$  for the direct band gap and  $m = 2$  for the indirect band gap. Band gap energy is obtained from the extrapolation of a plot of  $(\alpha h\nu)^m$  versus  $h\nu$ , also called the Tauc plot [35]. The band gap is classified by the direction of the electronic transition, where is a direct band gap if the k-vector of the highest point of the valence band match with the lowest point of the conduction band, if not, is classified as an indirect band gap.

### 1.3. Photoelectrochemical cell

Photoelectrochemical (PEC) cells are a technology based on artificial photosynthesis and a promising candidate to produce green hydrogen directly [31], [34], [36]–[40] as shown in Figure 1. The process using PEC devices was demonstrated to be very promising for producing clean and renewable hydrogen on large scale. The configuration of a PEC cell consists of two electrodes, an anode and a cathode, where at least one of them or both must be an n- or a p-type semiconductor (photoanode or photocathode, respectively), and a reference electrode immersed in an aqueous electrolyte solution. In our example (Figure 1), a photoanode, such as hematite, initiates the process by absorbing the incident radiation, where it must be sufficient to promote the electron from the valence band (VB) to the conduction band (CB), resulting in a generation of electron-hole pair. The hole is a minority carrier, and the electron is the majority carrier since a photoanode must be an n-type semiconductor. The hole must reach the surface for oxygen evolution reaction (OER) while the electrons are collected in the photoanode back contact and transferred to the counter electrode by an external system, and finally promote the hydrogen evolution reaction (HER) as shown in Figure 1[31], [37], [38]. Aiming the green hydrogen, the dream is to use sunlight as a source to activate de processes [36].

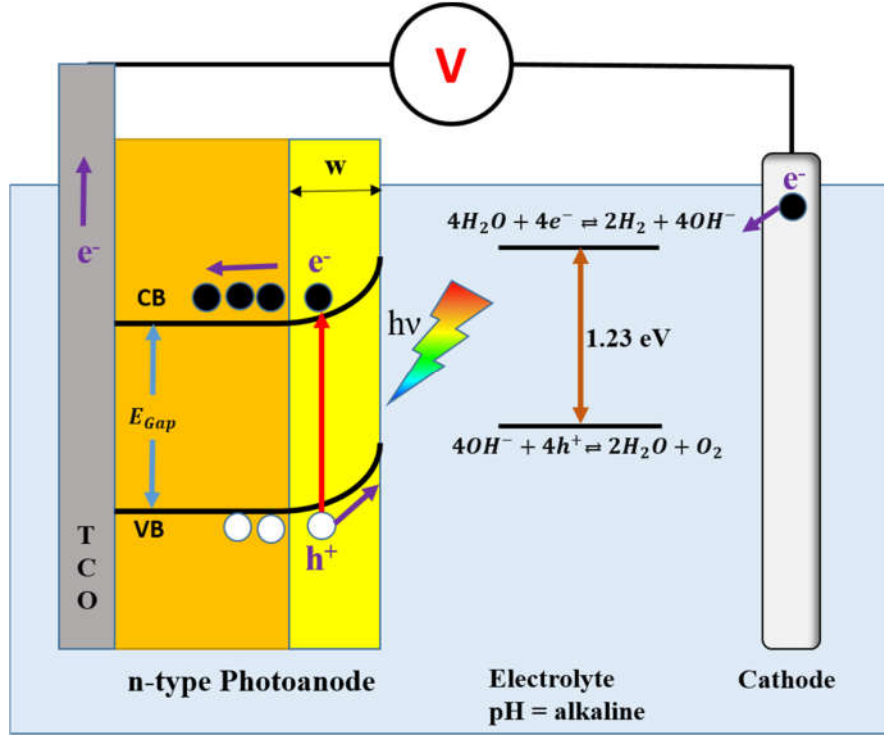
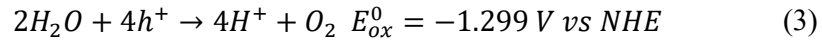
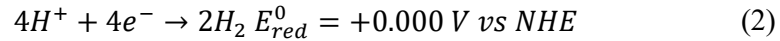
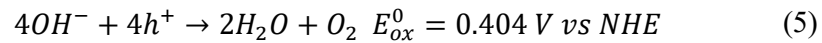
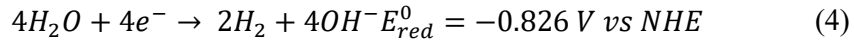


**Figure 1 - Scheme of a photoelectrochemical cell, composed of an n-type photoanode and a cathode immersed in an alkaline electrolyte. The OER and HER are shown for each process, according to the bandgap for solar to hydrogen conversion.**

As shown in Figure 1, the photoanode and the cathode are immersed in an aqueous electrolyte solution. The electrolyte can be acid or alkaline, which means that the environment of application depends on the pH. For an acid environment, the redox reaction can be written as:



If the environment is alkaline, the redox reaction can be written as



Considering that the OER is the bottleneck of the water splitting process because  $4h^+$  is necessary to generate one molecule of  $O_2$  and supply the electrons that are needed to HER, and the redox potential is more favorable for OER in alkaline media than in the acid, the PEC in the

alkaline environment is more common. However, several semiconductors have been studied as photoanode and also photocathodes, as well as their applications in both electrolytes. To facilitate the comparison of the performance of different photoelectrodes and standardized those regarding electrolytes with different pH, the potentials are often converted to a reversible hydrogen electrode (RHE), by the Nernst equation (6). The equation refers to a standard condition ( $T=298\text{ K}$ ), and herein the reference electrode was chosen as Ag/AgCl ( $E_{Ag/AgCl}^0 = 0.1976\text{ V}$ ).

$$E_{\text{RHE}}^0 = E_{\text{Ag/AgCl}}^0 + 0.059 \cdot \text{pH} \quad (6)$$

The bottleneck that makes the application of the PEC unfeasible is that any photoelectrode reaches the minimum efficiency. For this reason, the main challenge is to develop an ideal photoelectrode that absorbs sunlight, has low-cost production, be able to realize the water-splitting process, and obtains hydrogen by a clean and sustainable method [41], [42].

An ideal photoelectrode presents the following properties: to keep the dream to use sunlight radiation, the semiconductor must absorb in the visible spectrum. The semiconductor band gap energy needs to be narrowed to 2.0 eV [37], and the band-edges energy needs to be aligned with the redox potential of the water oxidation/reduction reaction to promote the oxygen evolution reaction and the hydrogen evolution reaction. Thermodynamically, the material needs to be stable in an aqueous environment. Moreover, to reduce production costs, the process needs to be simple, the minimum photocurrent predicted by literature is around  $10\text{ mA cm}^{-2}$  and be scalable. However, to date, the performance of any semiconductor, which fulfills the main requirements, has been limited by different issues such as poor transport, high recombination, or low charge carrier generation[43], [44].

Over years, different routes in the way bottom-up were developed to obtain nanostructures such as chemical bath deposition [45], electrochemical deposition [46], co-precipitation [47]–[56], electrospinning [57]–[59], sonochemical emulsification [60], microemulsion [1], [61], ultrasonic spray pyrolysis [62], [63], spin coating [64]–[67], atomic layer deposition [68], [69], chemical vapor deposition [70]–[73] plasma spray [74], sol-gel [75]–[81], solvothermal [82]–[84], and hydrothermal conditions [72], [85]–[90]. The synthesis method is an important parameter when the main goal is to develop the best morphology to perform the water splitting. Until now, any photoelectrode applied in PEC devices achieve the minimum efficiency needed for applications (10% STH) [41], [91].

#### 1.4. Iron Oxide

Cornell and Schwertmann (2003) discuss in detail the 16 types of iron oxides, which are composed of Fe bonds with O and/or OH [92]. Hematite ( $\alpha\text{-Fe}_2\text{O}_3$ ) is a semiconductor that has been studied due to its favorable properties to be applied as a photoanode in PEC devices.  $\alpha\text{-Fe}_2\text{O}_3$  is thermodynamically stable in an aqueous environment, earth-abundant, and nontoxic material that possesses a narrow band gap energy ( $\sim 2.2$  eV) which indicates an absorption range in the visible region of the spectrum [36], [38], [39], [44], [87], [93], [94]. The composition is based on abundant elements on earth that help to decrease the cost of production. Theoretically, the solar to hydrogen (STH) conversion efficiency for hematite, with a band gap energy of 2.2 eV, is 12.9% [95]. However, the state-of-the-art for pristine hematite achieved an STH efficiency of 3.1% [30], [96]. The difference between theory and experimental STH efficiency for hematite is due to the hematite problems such as the short hole diffusion length (2-4 nm) [36], [38], [43], [44], [94], [96]–[100], and also due to the low conductivity of the majority carriers [97].

The properties of hematite that are important to the PEC devices application were cited in the previous section, which explains why this material is a promisor candidate to be used as a photoanode. In counterpart, the unmodified hematite or pristine hematite, as well known, is not efficient by itself [39]. In a way to increase the hematite efficiency, strategies such as doping, the use of co-catalysts, morphology control, heterojunctions, and surface activation have been used to improve their photocurrent response [43].

For years, research groups have been studying many strategies to enhance hematite performance by controlling the parameters that govern the photocurrent ( $J_{\text{ph}}$ ). The main equation that incorporates the formalism described by Murphy et.al (2006) [95], which describes the photocurrent density as

$$J_{\text{ph}} = J_{\text{abs}} \times \eta_{\text{overall}} \quad (7)$$

the  $J_{\text{abs}}$  is the theoretical photocurrent density derived from absorbance properties (this is considered the maximum light absorbed that can be used in the STH conversion) [101] and  $\eta_{\text{overall}}$  is the overall photocurrent conversion efficiency [101]. The  $J_{\text{abs}}$  are estimated using the formalism described by Zandi and Hamann (2015) [102], which integrates the absorption spectra obtained from spectrophotometry measurement, the detailed equation is shown in

section 4.2.  $\eta_{\text{overall}}$  can be expressed by the product of the charge separation efficiency ( $\eta_{\text{sep}}$ ) and the catalytic efficiency ( $\eta_{\text{cat}}$ ) [101], [103].

The first parameter ( $J_{\text{abs}}$ ) of Eq. (7) is related to the morphology, and that implies the surface area since the redox reaction occurs in the solid/liquid interface as shown in Figure 2. The literature has reported that the best photocurrents are achieved with one-dimension morphology rod-like. As hematite has a problem of low diffusion of minority carriers, mesoporous nanostructures bring an interesting combination of properties that can decrease the path way of the minority carrier, which enhances the charge separation efficiency [94], [101], [104]. It is important to remember that the increasing of  $J_{\text{abs}}$  by increasing the photoelectrode thickness also brings more electronic defects that can trap the charge and decrease the overall efficiency. Nogueira et. al. (2019) presents a study with mesoporous hematite with different thickness, and as expected, the  $J_{\text{abs}}$  improve by increasing the thickness, in counterpart, the  $J_{\text{ph}}$  improves until the film thickness is  $\approx 200$  nm. Surpassing that thickness, the photocurrent decreases. In their case, the porosity impacts the  $J_{\text{ph}}$  by decreasing the absorption coefficient [66], [67], [94], [95], [101].

The charge separation efficiency ( $\eta_{\text{sep}}$ ) and catalytic efficiency ( $\eta_{\text{cat}}$ ), which governs the overall efficiency, are dependent on each other [105]. Figure 2 shows the scheme of the hematite photoelectrode, where the  $\eta_{\text{cat}}$  is the efficiency of the photoelectrode surface to promote the chemical reaction, and  $\eta_{\text{sep}}$  is the photoelectrode efficiency in separate the photogenerated charge. In this regard, researchers have been studying the addition of some elements to the periodic table [100]. However, some of them act as dopants, co-catalyst, or passivation agents [43], [44], [90], [98], [100], [101], which will be detailed further.

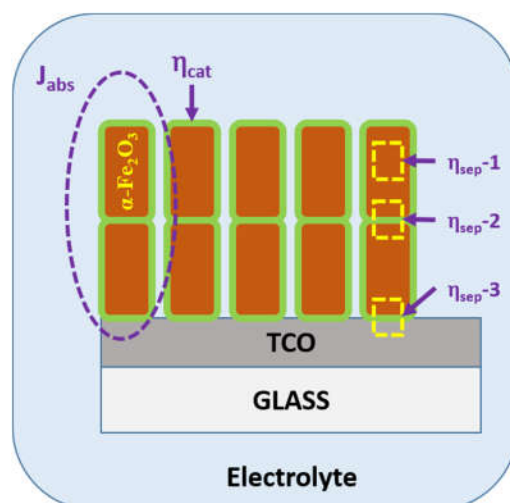


**Figure 2 - Scheme of photoanode and where the parameters of equation (2.6) impact.**

These parameters reveal some specific ‘signatures’ in the photoelectrochemical analysis given by a linear sweep voltammetry measurement. Figure 3 shows the grey solid line which represents the experimental curve of photocurrent versus applied potential. In the dashed black line (Figure 3), the photocurrent increases by improving the separation of the charge photogenerated via morphology control, which is related to  $J_{abs}$  and  $\eta_{sep}$  improvement. If a co-catalyst is added to pristine hematite,  $\eta_{cat}$  will improve, and there is a shift in the onset potential, as shown in the gray dot-line in Figure 3. In addition, when all the problems of hematite are solved, the solid black line represents the ideal hematite photoelectrode.

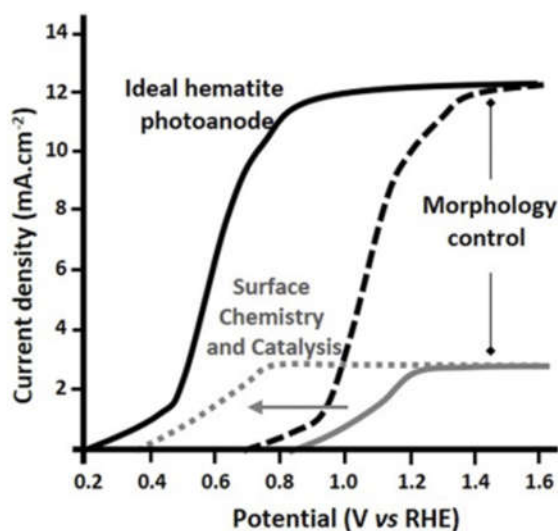


**Figure 3-  $J_{ph}$  of an ideal hematite photoanode (solid black line), a  $J_{ph}$  obtained experimentally (solid grey line), an improvement of  $\eta_{sep}$  (dashed black line), and an improvement of  $\eta_{cat}$  (dotted grey line). Adapted with permission from Sivula et al., ChemSusChem 4, 432–449 (2011). Copyright 2011 WILEY-VCH Verlag GmbH & Co.**



### 1.5. Hematite modifications

The benchmark for modified hematite-based photoanode is reported by Jeon et. al. (2017), where the photocurrent achieves  $\approx 6 \text{ mA cm}^{-2}$  at  $1.23 \text{ V}_{\text{RHE}}$  [106]. The authors used the hydrothermal condition to obtain one-dimensional morphology at the akageneite phase [106]. To achieve the highest photocurrent, a series of thermal treatments in different temperatures and times was performed in air and under  $\text{H}_2$  flow. Moreover, the incorporation of modifiers and co-catalyst onto hematite-based photoanode was also employed [106]. Linear sweep voltammetry measurement for 100 hours under illumination showed photoanode stability during operation [106].

This section will be discussing the improvement of  $\eta_{\text{sep-1}}$  and  $\eta_{\text{sep-2}}$ , shown in Figure 2. The literature has shown that the highest photocurrent was obtained from doped-hematite with the elements Ti [106], [107], Si [94], [108]–[110], and Sn [111], [112]. In a recent work, Souza Junior et. al. (2021) [100] give a perspective of doped-hematite with a single element, which highlights the improvement of the photocurrent response according to the location of the dopant. The discussion focusses on the dopant's location, such as in substitutional and homogeneously through the bulk, or at the grain surface, which can be in the solid/liquid interface or solid/solid interface (segregated in the grain boundaries). In each case, the dopant “works” in a different way resulting in an enhancement of electrical conductivity and consequently the photocurrent response.

It is well known that doping is a smart strategy to improve the conductivity of a semiconductor. In the case of doped-hematite, the amount of charge carrier (donor density –  $N_D$ ) increases, consequently, more charge will be able to provide the water splitting. However, the enhancement of  $N_D$  decreases the space charge layer ( $W$ ), which is the active region that contributes to the oxygen evolution reaction. This region is called the space charge layer or depletion layer ( $W$ ), given by Eq. (8)

$$W = \sqrt{\frac{2 \varepsilon_r \varepsilon_0 (V_{\text{RHE}} - V_{\text{fb}})}{e N_D}} \quad (8)$$

where  $e$  is the electron charge,  $\varepsilon_r$  is the dielectric constant (80 for pristine),  $\varepsilon_0$  is the vacuum permittivity,  $V_{\text{RHE}}$  is the applied potential, and  $V_{\text{fb}}$  is the flat-band potential [34], [39], [100]. Although, the  $W$  width decrease, the lifetime of the carriers also increases, which combines

with  $N_D$  resulting in an enhancement of photocurrent response [100], [113]. This strategy is shown schematically in the second and third quadrants in Figure 4.

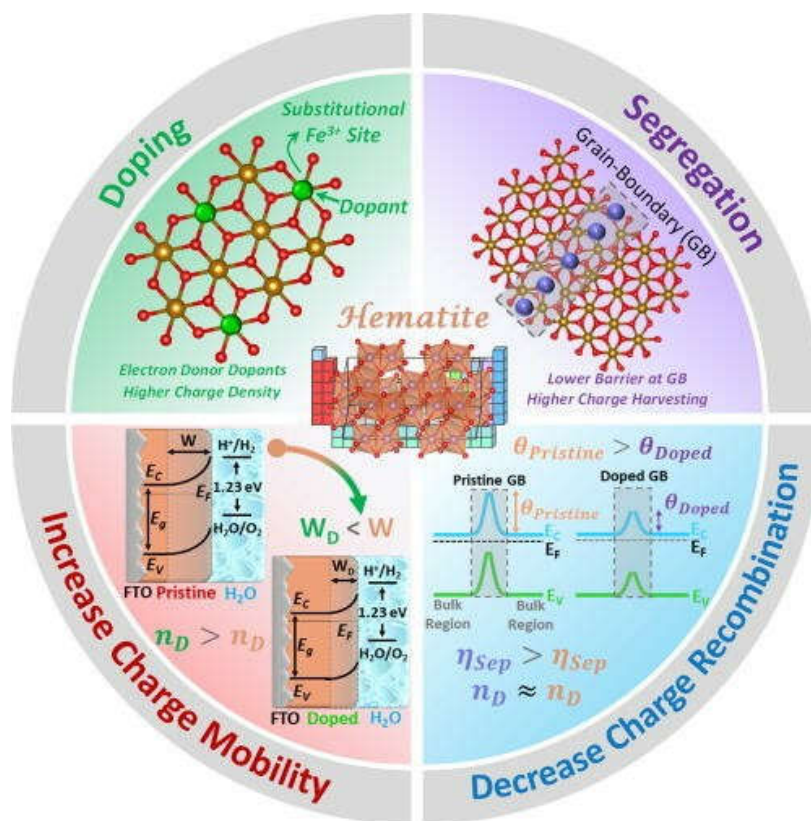


**Figure 4 - Scheme of the strategies of doped hematite according to the location of element doping.**  
**Published in:** Joao B. Souza Junior; Flavio L. Souza; Lionel Vayssieres; Oomman K. Varghese;  
**Appl. Phys. Lett.** 119, 200501 (2021). Copyright © 2021 Author(s)

Souza Junior et. al. (2021) [100] also discuss the elemental doping on the surface of the grain and/or in the grain boundaries, also called segregation. To understand the impact of region/location of the element doping, the authors make a comparison between a single crystal and polycrystalline hematite. For a single crystal, the charge carrier flow in the bulk with low recombination, and the addition of elemental doping increases the  $N_D$ . In the case of a polycrystalline, the main problem is the high recombination of carriers in the grain boundaries. The strategy to add elements doping in the grain boundaries impacts decreasing the energy barrier, which improves charge separation efficiency ( $\eta_{sep}$ ) and improves the photocurrent response, as shown in the first and fourth quadrants in Figure 4. This strategy is interesting due to the best performance of photocurrent is achieved without changing the  $W$ .

The enhancement of modified-hematite photoanode by the addition of elements became hard to understand since the single impact of these elements. At low concentration of  $Ti^{4+}$  as a

modifiers, the elements can doping the bulk which result in the decrease of the  $W[100]$ , [113]. In the case of Sn, this element is present in the transparent conductor layer, which is composed of fluorine-tin oxide (FTO). Studies show that the Sn auto diffuses to hematite due to the high temperature of annealing (773-1073 K) [100], [104]. The main problem with using Sn is understanding what the main contribution of the Sn is provided by the FTO and the Sn incorporated intentionally in the grain boundaries of hematite since both can impact the photocurrent response.

### 1.5.1. Modifier: Antimony on Hematite

Hussak and Prior (1897) published the first report of Iron mixed with Antimony (Sb) where they discovered Tripuhyite ( $\text{FeSbO}_4$ ) [114]. They observed for the first time in the cinnabar-bearing gravel of Tripuhy, found in Ouro Preto, Minas Gerais, Brazil [114]. However, crystallographic studies were just reported in 1955 by Manson and Vitaliano [115]. They proposed that Fe and Sb are combined to form  $\text{FeSbO}_4$ , which crystallizes in a tetragonal lattice [115].

Although there are reported different studies related to Fe/Sb system, to date, only three papers detailed the impact of Sb on hematite photoanode for water splitting applications. Annamalai et al. (2018) presented the pristine hematite with so-called ‘ex-situ Sb doping’, which used the hydrothermal synthesis to obtain a film of metastable phase  $\beta\text{-FeOOH}$ , and subsequently, the Sb was added via dip-coated followed by annealing (800°C for 10 minutes) to activate the hematite [116]. They reported that the best ex-situ  $\text{Sb}^{+5}$  doping on hematite photocurrent is  $1.1 \text{ mA cm}^{-2}$  at  $1.23 \text{ V}_{\text{RHE}}$ . The incorporation of Sb on hematite was confirmed by X-ray photoelectron spectroscopy (XPS). They concluded that the incorporation of Sb increases the donor density carrier ( $N_D$ ), however, the most impact was due to the enhanced wettability and catalytic active sites, and the large negative surface charge.

Nevertheless, the state-of-the-art hematite modified with Sb incorporation belongs to the work of Nogueira et al. (2019) [101]. The method that was used is a combination of the colloidal nanocrystal deposition (CND) process with dip-coating assisted by a magnetic field to obtain both unmodified hematite and Sb-modified hematite [101]. They reported that the best Sb-modified hematite photocurrent density is  $1.68 \text{ mA cm}^{-2}$  at  $1.23 \text{ V}_{\text{RHE}}$ . Comparing the  $\eta_{\text{global}}$ , the Sb incorporation enhanced this parameter by a factor of 4.5, and the  $J_{\text{ph}}$  increase by a factor of 6.5, for samples in the same condition. The authors concluded that the improvement is related

to the enhancement of the charge separation efficiency ( $\eta_{\text{sep}}$ ), due to the Sb being located preferentially in the porous surface and the grain boundary (GB). The role of Sb in the GB is decreasing the voltage barrier, which results in an improvement of electrical conductivity.

Lima et. al. (2021) in a theoretical study, uses the density functional theory calculation to explain the effect of Tin (Sn) and Antimony (Sb) segregation on the hematite solid-liquid interface and at grain boundaries [117]. The author shows an enhancement on the charge transport inter-grain of hematite due to the lower potential barrier, when the elements segregates at the grain boundaries. On the solid-liquid interfaces, the dopants reduce the oxygen vacancy formation, which increases the flat-band potential [101], [116], [117].

### **1.5.2. Modifier: Zirconium oxide (ZrO<sub>2</sub>) on hematite**

The morphology of the photoanode impacts the photocurrent response due to the length of the depletion layer [118]. Li et. al. (2017) showed that the nanotube structures have much better performance over nanorods for charge separation [118], [119]. The authors obtained the nanotube structure by incorporating Zirconium Oxide (ZrO<sub>2</sub>) as a shell in the metastable phase  $\beta$ -FeOOH, which was obtained by hydrothermal synthesis [119]. The ZrO<sub>2</sub> was incorporated into the  $\beta$ -FeOOH by atomic layer deposition and subsequently submitted to a high-temperature calcination step [119]. The photocurrent response obtained was 1.5 mA cm<sup>-2</sup> at 1.23 V<sub>RHE</sub> without any co-catalyst, and 1.87 mA cm<sup>-2</sup> with Co-Pi, also in 1.23 V<sub>RHE</sub>, which is the state-of-the-art for this photoelectrochemical application.

### **1.5.3. Modifier: Hafnium on hematite**

The ion Hafnium IV (Hf<sup>4+</sup>), significantly improves the photocurrent to values consistent with the recent literature exploring Hf incorporation [120]. Ma et. al. 2022, showed an increased photocurrent (1.79 mA cm<sup>-2</sup>) in compare to the pristine hematite by Hafnium incorporation. The authors used an in-situ method, which consists of insert the element into the aqueous precursor solution. The hydrothermal conditions were used to synthesize the photoelectrodes followed by fast heat treatment (1073 K for 10 minutes). Different concentrations of Hf were used in this study, and the best condition that obtained the higher photocurrent was by adding 0.25 mM. The work concludes that the Hf doped the hematite, which an increase of the donor density is responsible to enhance the charge separation efficiency.

### **1.6. Mitigation of the electron loss at fluorine-doped tin oxide/photoelectrode interface**

Taking a look at the majority carriers (electrons for hematite case), the charge photogenerated was collected at the back contact (FTO/photoelectrode interface,  $\eta_{sep-3}$  in Figure 2). However, at FTO/photoelectrode interface has some problems such as roughness, which implies an incompatibility of electronic and/or structural interactions [66], [121], [122]. To minimize this problem, the strategy is to insert an ultrathin layer to decrease the roughness of TCO, and also block the flow-back of the charge collected to the electrolyte [121], and consequently lose the charge. Some studies have been demonstrating the efficiency of this strategy by incorporating blocking layers of  $SiO_x$  [123],  $Ga_2O_3$  [124],  $Nb_2O_5$  and  $TiO_2$  [121], and  $ZrO_2$  [125].

The growth process in hydrothermal conditions permits grow the morphology in both peaks and valleys of the FTO, but the film is mesoporous, and consequently, the FTO is still exposed to the electrolyte. In this way, the use of a blocking layer is a promising strategy to avoid this problem.

## 2. ORIGINALITY AND CHALLENGES OF THE PROJECT

The originality of this work is to reduce some steps of the synthesis to obtain the photoanode to turn the methodology available to scale up the photoelectrode area without losing efficiency. To improve the efficiency of Hematite, tetravalent element such as Hafnium ( $\text{Hf}^{4+}$ ), Zirconium ( $\text{Zr}^{4+}$ ), and a pentavalent element, Tantalum ( $\text{Ta}^{5+}$ ), will be incorporated into Hematite.

The challenge is to improve the efficiency and reduce the complexity of the synthesis. Using hydrothermal conditions with low temperature and low pressure is a way to reduce the cost of production and keep the method reproducible.

### 3. OBJECTIVES

Following the background, the bottleneck for photoelectrochemical cell application is the high cost and the low efficiency. One of the most costs of serial production belongs to the level of complexity of the synthesis process adopted. In the study reported by Jeon et.al (2017), the highest photocurrent material achieves  $\approx 6 \text{ mA cm}^{-2}$ , however, the procedure adopted to obtain the films is impracticable in serial production due to the high cost of setup and the raw material.

In this way, the general objective of the present work is to reduce the complexity of the synthesis route using hydrothermal conditions, which is a method that is available for industrial [105], without losing efficiency. Then, to improve the efficiency of the photoanode, some modifications with Hafnium (Hf) and Zirconium (Zr) were carried out at different moments of the fabrication of the photoanode.

## 4. EXPERIMENTAL SECTION

### 4.1. Synthesis of photoelectrodes

#### 4.1.1. Substrate properties and cleaning process

The substrate used is an alumino-borosilicate glass (thickness: 1.1 mm) coated with fluorine-doped tin oxide (FTO,  $10 \Omega \text{ square}^{-1}$ ) layer purchased from Solaronix SA. The FTO has been subjected to a cleaning process that consists of four baths of 30 minutes each in boiling deionized water (resistivity greater than  $18.2 \text{ M}\Omega \text{ cm}$ ) with and without the addition of 10%  $v/v$  of Extran, respectively, acetone, and isopropyl alcohol, which the last two were heated below their boiling points at 323 and 348K, respectively.

#### 4.1.2. $\alpha\text{-Fe}_2\text{O}_3$ Synthesis procedure

Hematite-based photoanode was designed via a controlled aqueous solution under hydrothermal conditions. An aqueous precursor solution (PS) was prepared by dissolving 0.15 M of ferric chloride ( $\text{FeCl}_3 \cdot 6\text{H}_2\text{O}$ ) (Sigma Aldrich, 98%), 1.0 M of sodium nitrate ( $\text{NaNO}_3$ ) (Sigma Aldrich, 99%), and set the pH in 1.5 by HCl. Deionized water (resistivity greater than  $18.2 \text{ M}\Omega \text{ cm}$ ) was used as a solvent in the PS. In a Teflon vessel of 60 mL of capacity, 30 mL of PS was added with FTO fixed in a holder, as shown in Figure 5. All of this apparatus was placed in a stainless-steel autoclave. The autoclave was placed in a conventional oven preheated to a given temperature. After a certain time, the autoclave is takeout from the oven and placed in an ice bath to cool down for 15 minutes. Subsequently, the FTO was washed with pure water to remove the residual salts.

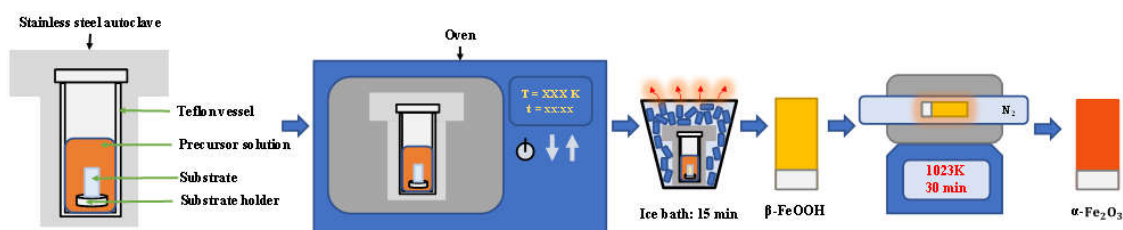


Figure 5 - Scheme of the hydrothermal process, from left to the right side we start with the allocation of the precursor solution and the substrate in the Teflon vessel and insert them in the autoclave. Afterward, we have the film growth under hydrothermal conditions following the ice bath, in which first we obtain the  $\beta\text{-FeOOH}$  phase and after the heat treatment the hematite phase.



The hematite ( $\alpha\text{-Fe}_2\text{O}_3$ ) phase and surface activation [70], were obtained after heat treatment (HT) at 1023K for 30 minutes under  $\text{N}_2$  flux. All the following procedures are shown in Figure 5.

#### 4.1.3. Modifiers addition

The modifiers such as Hf, Ta, and Zr were incorporated by spin coater (Laurell, WS-650MZ-23NPP) working at 500 rpm for 10s was used to deposit 50 $\mu\text{L}$  an ethanol-based solution of 0.02 M over the  $\beta\text{-FeOOH}$  coated FTO, as shown in Figure 6. The reactants used were Hafnium(IV) chloride (Sigma Aldrich, 98%), Tantalum(V) isopropoxide (Alfa Aesar, 99.9%), and Zirconium(IV) oxynitrate hydrate (Sigma Aldrich, 99%).

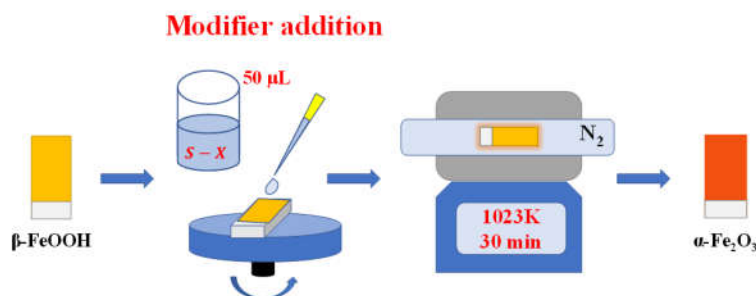


**Figure 6 - Scheme of modifier addition.** Onto the film in the  $\beta\text{-FeOOH}$  phase, we deposited 50  $\mu\text{L}$  of the modifier solution via spin coating, and then the same process followed as previously said.

#### 4.1.4. Blocking layer coating

The blocking layer (BL) was designed by adding 0.01M of an ethanol solution of a selected salt. A spin coater from Laurell (WS-650MZ-23NPP) was used for the deposit of 50 $\mu\text{L}$  of the ethanol solution at 2000 rpm for the 20s onto the clean FTO substrates twice, as shown in Figure 7. The coated FTO was annealed in air at 573K for 1 hour before the immersed into the  $\beta\text{-FeOOH}$  precursor as detailed above. The reactants used were Aluminum 2,4 pentanedionate (Alfa Aesar), Hafnium(IV) chloride (Sigma Aldrich, 98%), Niobium(V) chloride (Sigma Aldrich, 99.9%), Tantalum(V) isopropoxide (Alfa Aesar, 99.9%), Titanium(IV) butoxide (Sigma Aldrich, 97%), and Zirconium(IV) oxynitrate hydrate (Sigma Aldrich, 99%).

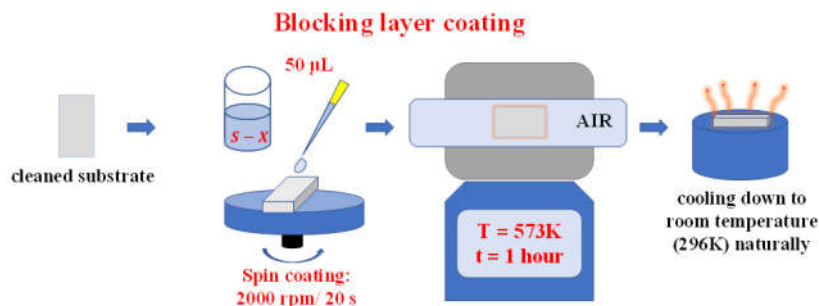


**Figure 7 - Scheme of blocking layer design.** Onto an already cleaned substrate, we deposited 50  $\mu\text{L}$  of the solution of the element via spin coating, this procedure is repeated twice, and then the substrate coated is subjected to thermal treatment and cooling down to room temperature ( $\sim 296\text{K}$ ) naturally.

#### 4.2. Optical properties

Spectrophotometric measurements were performed in the wavelength range from 220 to 800 nm, which covers the entire visible spectrum. The spectrophotometer is a SHIMADZU UV-3600 Plus, with an integrating sphere coupled. The band gap was obtained by using the formalism detailed in section 1.2. The theoretical photocurrent density derived from absorbance properties (maximum light absorbed in the solar to hydrogen conversion) ( $J_{\text{abs}}$ ) is estimated by using Eq. (9).

$$J_{\text{abs}} = -q \phi (\eta_{\text{LH}}) \quad (9)$$

where  $q$  is the elemental charge,  $\phi$  is the photon flux, and  $\eta_{\text{LH}}$  is the light-harvesting efficiency.

#### 4.3. Photoelectrochemical characterization

A standard 3-electrode cell configuration was used to perform the photoelectrochemical characterization, in which the hematite photoelectrode is the working electrode, the counter electrode is a Platinum wire, and a reference electrode is Ag/AgCl. The electrolyte is a solution with 1.0M of sodium hydroxide (Sigma Aldrich, 98%). The cell was illuminated with a xenon lamp-based solar simulator (Oriel 67005, 150 W) coupled with a standard air mass 1.5 global filter (AM 1.5 G). The sunlight power simulation ( $100 \text{ mW cm}^{-2}$ ) was set by a photodetector (photodiode power sensor from Newport, which further the photoelectrode will be positioned).

Linear Sweep Voltammetry (LSV) was carried out with a scan rate of  $0.05 \text{ V s}^{-1}$ , using an AutoLab PGSTAT128N. The applied potential was converted into the reversible hydrogen electrode (RHE) by Eq. (5). Cyclic voltammetry (CV) measurements were recorded from 0.7 to 1.6  $\text{V}_{\text{RHE}}$ , using a scan rate of  $10.0 \text{ mV s}^{-1}$ . Cleaned FTO and FTO coating with  $\text{ZrO}_2$

underlayer were immersed in 1.0 M KOH containing 10 mM  $K_4[Fe(CN)_6]$  electrolyte solution. The intrinsic properties such as donor density carrier ( $N_D$ ), flatband potential ( $V_{fb}$ ), and space charge layer ( $w$ ) were investigated by Mott-Schottky (M-S) plot obtained from electrochemical impedance spectroscopy (EIS) measurements. The EIS was performed with the same setup of LSV in dark conditions and using a Frequency Response Analyser (FRA32M) module. M-S plot was extracted in the linear region at the frequency of 1.0kHz. The  $N_D$  was estimated from Eq. (10), which is proportional to the inverse slope of the linear fitting of the M-S plot.

$$\frac{1}{C_{SC}^2} = \frac{2}{\epsilon_0 \epsilon_r e N_D A^2} ((V_{RHE} - V_{fb}) - \frac{kT}{e}) \quad (10)$$

where  $C_{SC}$  is the capacitance of the semiconductor space-charge layer,  $\epsilon_r$  is the dielectric constant,  $\epsilon_0$  is the vacuum constant,  $e$  is the elementary charge,  $k$  is the Boltzmann constant, and  $T$  is the temperature.  $W$  was estimating from Eq. (8)

$V_{fb}$  was determined by the Gärtner-Butler [126] approximation with  $H_2O_2$  as a hole scavenger. 5% of  $H_2O_2$  was added to the electrolyte (NaOH, 1M) to perform an LSV measurement. A plot of  $J_{ph}^2$  versus applied potential (RHE), reveals the  $V_{fb}$  when the linearly extrapolate intercepts with the x-axis.

#### 4.4. Structural and morphological characterization

X-ray diffraction patterns were characterized with a Bruker, D8 Advance ECO using  $CuK\alpha$  radiation ( $\lambda = 0.15406$  nm). The  $2\theta$  range scanned was from  $10^\circ$  to  $90^\circ$  with a step scan of  $0.02^\circ$ . Standard card files from the Joint Committee on Powder Diffraction Standards (JCPDS) were used to identify the crystal structure of the samples.

The morphology was characterized by a dual beam electron microscope combining a scan electron microscope (SEM) with a focused ion beam microscope (FIB, Scios 2 DualBeam) from Thermo Fisher Scientific. The images were analyzed using ImageJ software. Surface roughness was evaluated by atomic force microscopy (AFM), NX-10 Park Systems in the intermittent contact mode (tapping mode) with silicon probe Nano World, FMR model, resonance frequency (nominal) 75 kHz, Force Constant (nominal) 2.8 N/m. A scanning image area of  $2 \times 2$  micrometers with a resolution of  $512 \times 512$  pixels was recorded. The Root Mean Square (RMS) of a surface measured was determined with Gwyddion Software.

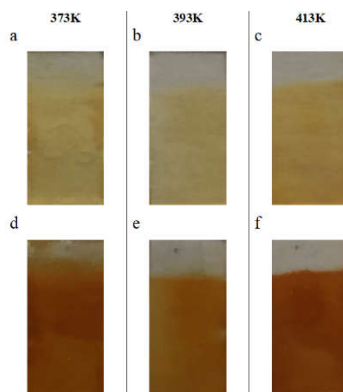
#### 4.5. Photoelectrodeposition of cocatalyst

NiFeO<sub>x</sub> cocatalysts were inserted by photoelectrodeposition on the films via immersion of the films in a pH 5.3 aqueous solution consisting of 16.0-mM NiSO<sub>4</sub>·6H<sub>2</sub>O (Sigma Aldrich, 99.9%), 5.0-mM Fe<sub>2</sub>(SO<sub>4</sub>)<sub>3</sub>·H<sub>2</sub>O (Sigma Aldrich, 97%), and 0.1-M NaCH<sub>3</sub>COO·3H<sub>2</sub>O (Sigma Aldrich, 99%). The same apparatus used to perform the linear sweep voltammetry (LSV) analysis was used, which is composed of a commercial (Metrohm Autolab) Ag/AgCl reference electrode, a platinum electrode as a counter electrode, and the film as the working electrode. Then, one LSV was performed from 0.5 to 0.9 V<sub>RHE</sub>, at a scan rate of 10 mV s<sup>-1</sup>, under simulated sunlight illumination of 100 mW cm<sup>-2</sup>. No additional thermal treatment was employed for the NiFeO<sub>x</sub> as-prepared films.

## 5. RESULTS

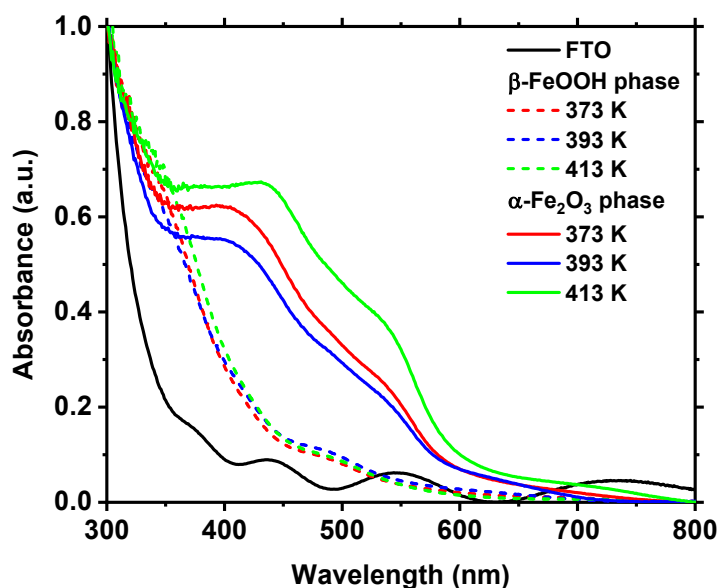
### 5.1. Hematite

Hydrothermal conditions were optimized by setting the synthesis time to 2 hours and varying the hydrothermal temperature (373K, 393K, and 413K). After the hydrothermal procedure, it can be noticed that the films have slight differences. All films present a yellow-brown color characteristic of the metastable iron oxyhydroxide phase named Akaganeite ( $\beta$ -FeOOH) as observed in Figure 8 a-c. After the heat treatment (HT), the films (Figure 8 d-f) presents a red color related to the Hematite ( $\alpha$ -Fe<sub>2</sub>O<sub>3</sub>) phase.



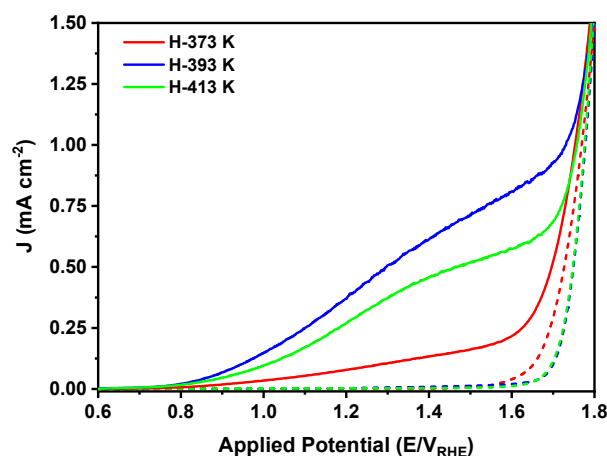
**Figure 8 - a, b, and c shows the as-prepared  $\beta$ -FeOOH obtained after hydrothermal synthesis at 373, 393, and 413 K respectively. d, e, and f show the photoelectrode after thermal treatment.**

Figure 9 shows the spectrophotometry analysis of the FTO (black line), The thin film before (dash lines), and after thermal treatment (solid lines). The successful phase transformation after thermal treatment can be confirmed for UV-Vis in which a change in the absorption properties is observed. For  $\alpha$ -Fe<sub>2</sub>O<sub>3</sub>, normally obtained after thermal treatment, the samples show a peak absorption of 550 nm, which lies in the visible light range. The estimated optical bandgap of samples is  $2.14 \pm 0.01$  eV, indicating that the materials are absorbing on visible light spectrum in agreement with previous reports.



**Figure 9- Spectrophotometry spectrum of the fluorine-doped tin oxide (FTO) glass substrate, and of samples for the Akaganéite phase (dash lines) and Hematite phase (solid lines).**

The photocurrent density ( $J_{ph}$ ) versus applied potential (in reversible hydrogen electrode – RHE) was obtained from linear sweep voltammetry (LSV) measurements under dark and 1 sunlight ( $100 \text{ mW cm}^{-2}$ ) illumination conditions (Figure 10). Under the dark condition (dashed lines), no current was observed, except in electrocatalysis potentials  $\sim 1.6 \text{ V}_{RHE}$ . Under illumination (solid lines), a photocurrent density can be observed after the photocurrent onset potential, approximately  $0.8 \text{ V}_{RHE}$ , demonstrating the hematite photoactivity. The best photocurrent at  $1.23 \text{ V}_{RHE}$  was obtained for the film synthesized at hydrothermal conditions set at 393 K for 2 hours. Following the theory discussed in Figure 3, the behavior of the hematite synthesized at 393 K (solid line in blue) compared to the one synthesized at 373K (solid line in red), suggesting better morphology control for the first film probably related to nanorod [87] diameter or/and length which consequently improve the photocurrent response. Considering the photocurrent density, hematite films used in the next sections were synthesized under hydrothermal conditions set at 393 K for 2 hours.



**Figure 10 - Linear Sweep Voltammetry curves under light, calibrated at  $100 \text{ mW cm}^{-2}$ , and dark conditions in NaOH (1.0 M) aqueous solution.**

X-ray diffraction analysis confirms hematite formation after thermal treatment, where the diffraction patterns were indexed to the hematite phase ( $\alpha\text{-Fe}_2\text{O}_3$ , JCPDS card 033-0664), as shown in Figure 11. An asterisk (Figure 11) indicated additional diffraction peaks associated with Cassiterite ( $\text{SnO}_2$ , JCPDS card 041-1445) phase from the FTO. Calculated Lotgering factor [127] ( $f = 0.44$ ) revealed preferential growth at (110) directions, which is well known that the preferential orientation is induced from FTO [128]. The crystallite size estimated from the Scherrer equation [129] was  $32 \pm 2 \text{ nm}$ . The cell parameters were calculated as  $a = 5.03 \pm 0.001 \text{ \AA}$ ,  $c = 13.74 \pm 0.01 \text{ \AA}$ , and  $V = 301.7 \pm 0.35 \text{ \AA}^3$ , the parameters corroborate with card JCPDS-033-0664.

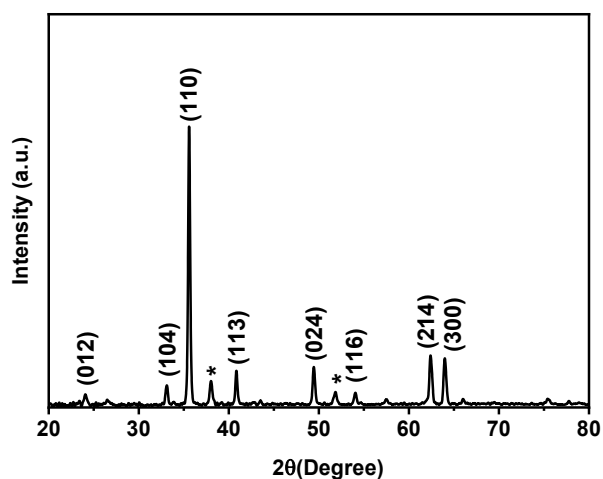


**Figure 11 - X-ray diffraction of the sample synthesized under hydrothermal conditions at 393K for 2h followed by a thermal treatment in an  $\text{N}_2$  atmosphere.**

The morphology of the nanorod array was confirmed with FIB-SEM analysis of the top and cross-sectional view, as shown in Figure 12 c and b, respectively. The average film thickness was  $500 \pm 30$  nm and the average rod diameter was  $54 \pm 11$  nm. Also, a topographic image was performed by AFM measurement, where the root mean square (RMS) roughness was 102 nm.

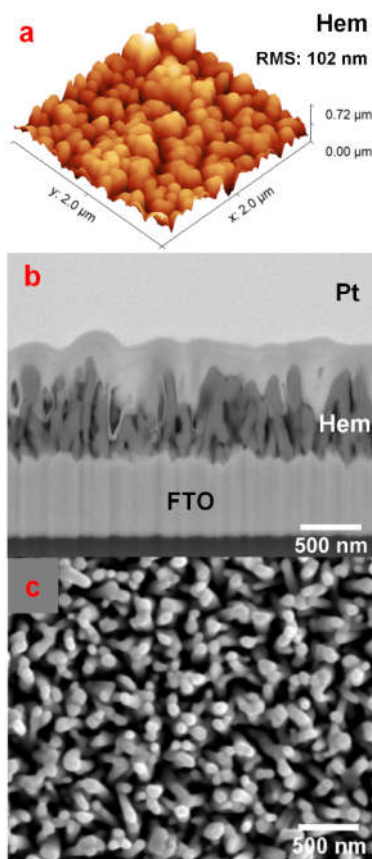


**Figure 12 – a) AFM measurement and the respective roughness of hematite thin films synthesized under hydrothermal conditions at 393K for 2h followed by a thermal treatment in an N<sub>2</sub> atmosphere. b) FIB-SEM image of the cross-section view, and c SEM image of the top view.**

## 5.2. Hematite modification

### 5.2.1. Element addition

From this stage, all samples were synthesized by hydrothermal conditions of 393 K for 2 hours followed by thermal treatment at 1023 K which were successfully characterized as hematite phase as observed in previous results. In order to improve the hematite photoresponse, the ions  $\text{Hf}^{4+}$ ,  $\text{Ta}^{5+}$ , and  $\text{Zr}^{4+}$  were incorporated into the photoelectrode according to the process detailed in the experimental section (4.1.3). The samples were named with a ‘Hem’ related to



the pristine hematite phase, followed by the modifier symbol (HHf, HTa, and HZr). The photoelectrodes were first characterized by spectrophotometry measurement (Figure 13), in which no additional band absorption was observed. From the UV-Vis spectra and using Eq. (9), the maximum theoretical photocurrent density ( $J_{\text{abs}}$ ) of each sample were  $8.8 \pm 0.2$ ,  $7.6 \pm 0.1$ ,  $8.3 \pm 0.3$ , and  $8.1 \pm 0.2 \text{ mAcm}^{-2}$  for Hem, HHf, HTa, and HZr respectively, where the  $J_{\text{abs}}$  slightly decrease for the modifier photoelectrodes.

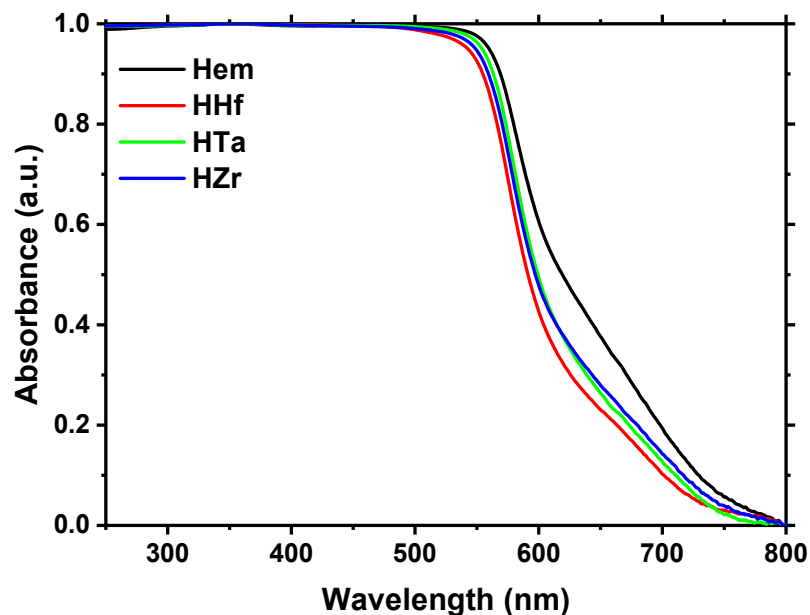


**Figure 13 - Spectrophotometry of Hem, HHf, HTa, and HZr.**

Figure 14 shows the photocurrent density ( $J_{\text{ph}}$ ) versus the applied potential of Hem, HHf, HTa, and HZr, obtained from linear sweep voltammetry (LSV) measurement. The highest  $J_{\text{ph}}$  at  $1.23 \text{ V}_{\text{RHE}}$ , was obtained after  $\text{Hf}^{4+}$  addition. A photocurrent onset shift at more positive potential is observed after modifiers addition, which has been associated with the creation of additional surface defects [100], [130]. Interestingly, the presence of  $\text{Hf}^{4+}$  also enhances the electrocatalytic activity of hematite as observed in the LSV curves measured in dark conditions. Analyzing the results obtained from the triplicate samples, it can be concluded that the methodology is robust and reproducible.

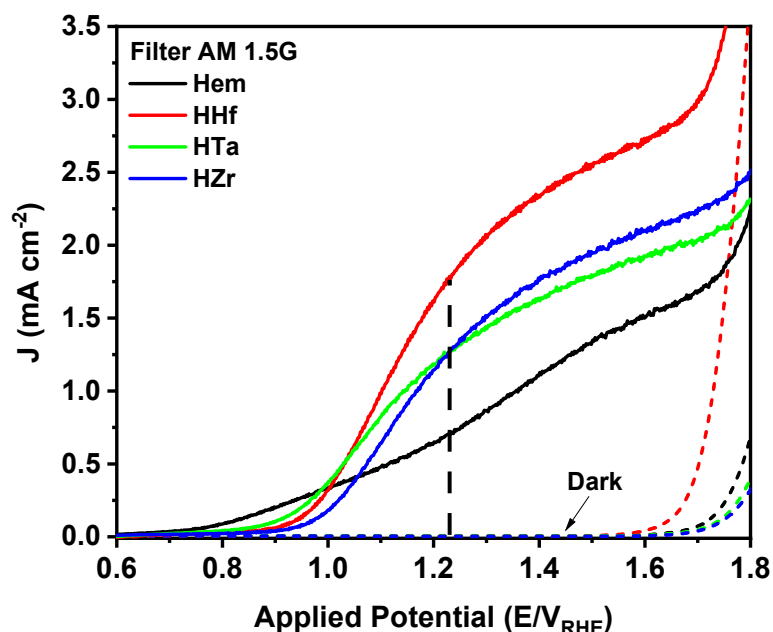


Figure 14 - Linear Sweep Voltammetry analysis of H, HHf, HTa, and HZr under light calibrated at  $100 \text{ mW cm}^{-2}$  and dark conditions in NaOH (1.0 M) aqueous solution.

The triplicates samples of Hem, HHf, HTa, and HZr, for both spectrophotometry and LSV analysis indicate that the sample is reproducible, as shown in Figure 15.

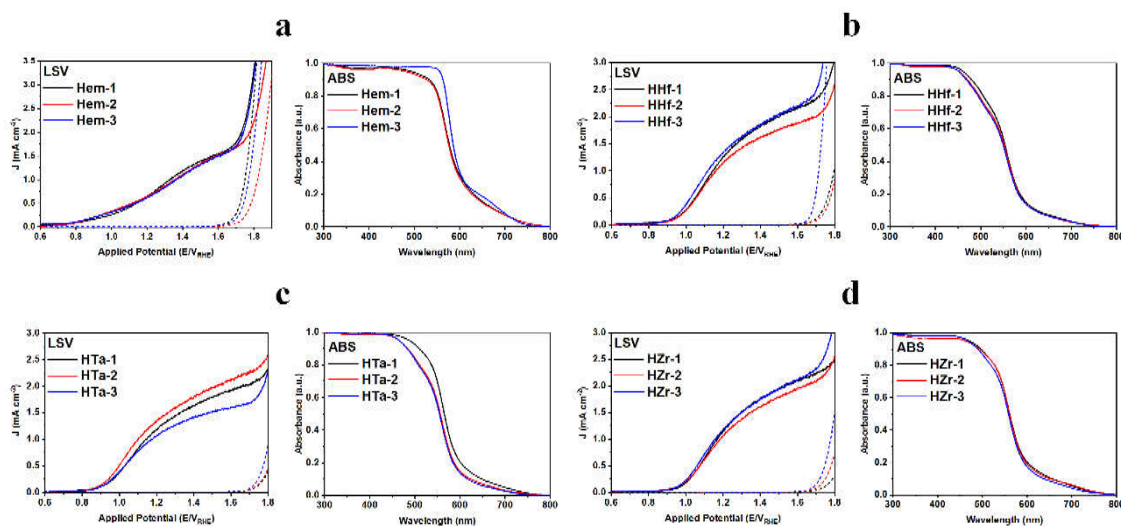
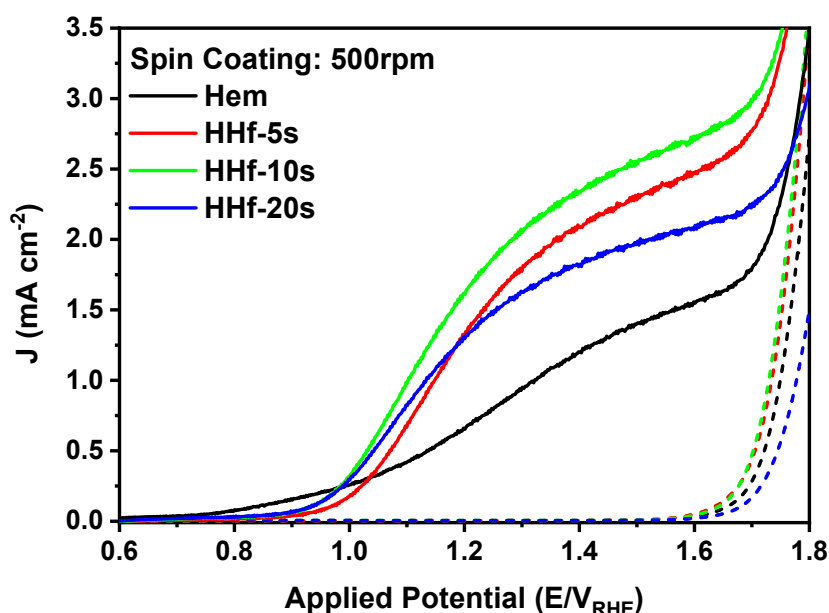


Figure 15 - Spectrophotometry and linear sweep voltammetry data of the triplicate for: a Hem, b HHf, c HTa, and d HZr.

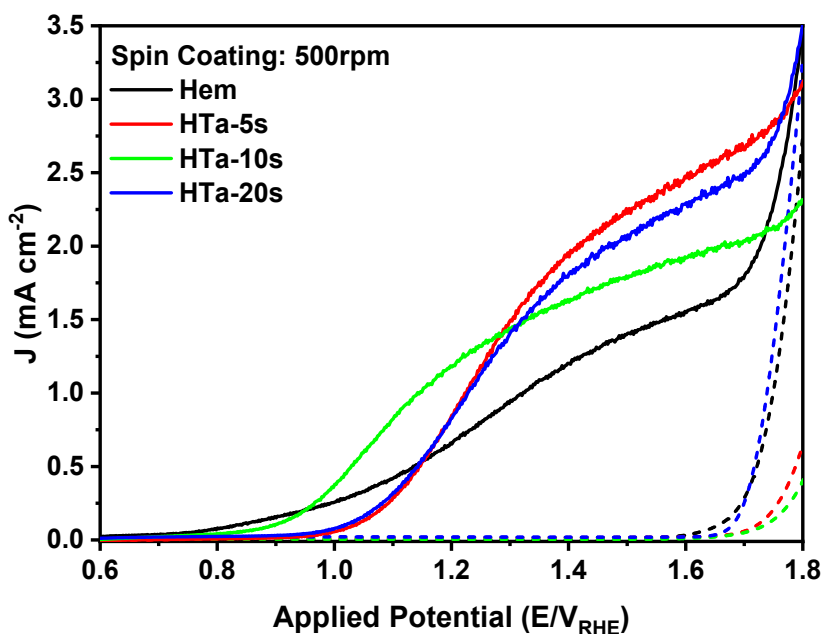
Since the amount of modifier deposited cannot be fully controlled by spin coating, optimizing the spin coating parameter represents an important step for synthesizing highly efficient films through this methodology. In this way, the spin coating parameters were

optimized by setting the rotation at 500 rpm and varying the time (5, 10, and 20 s) using the same precursor solution concentration (20 mM). Figure 16 shows the photocurrent response for pristine hematite (Hem), and for the  $\text{Hf}^{4+}$  addition by spin coating optimization, where the samples were named HHf-5s, HHf-10s, and HHf-20s, according to the time. The highest photocurrent response was obtained with the spin coating set at 500 rpm for 10s, where the obtained photocurrent response was 0.75, 1.48, 1.80, and 1.42  $\text{mA cm}^{-2}$  at 1.23  $V_{\text{RHE}}$  for Hem, HHf-5s, HHf-10s, and HHf-20s, respectively. A positive onset shift on photocurrent is more pronounced for HHf-5s, which is the time to expect to have a higher amount of  $\text{Hf}^{4+}$ , consequently, the surface states increase. In counterpart, the photocurrent response of HHf-5s is higher than the HHf-20s, indicating that the presence of  $\text{Hf}^{4+}$  influences the charge separation.



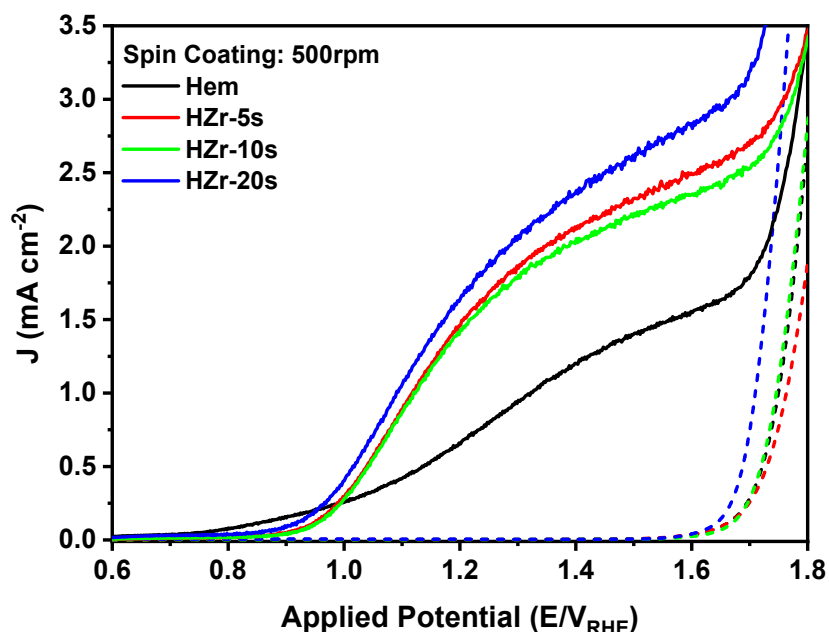
**Figure 16 – Linear sweep voltammetry analysis for spin coating optimization for  $\text{Hf}^{4+}$  addition under light calibrated at  $100 \text{ mW cm}^{-2}$  and dark conditions in NaOH (1.0 M) aqueous solution.**

Figure 17 shows the photocurrent response as a function of the applied potential of spin coating optimization for  $\text{Ta}^{5+}$  addition. Similar to Hf, the samples are named HTa-5s, HTa-10s, and HTa-20s. There is a pronounced positive shift in the onset potential for HTa-5s and HTa-20s, indicating that there are more surface states under these conditions. HTa-10s shows an onset potential less pronounced, however, the charge separation decrease at higher potentials indicating that the material is saturated. The photocurrent response were 0.75, 1.03, 1.28, and 1.01  $\text{mA cm}^{-2}$  for Hem, HTa-5s, HTa-10s, and HTa-20s respectively.



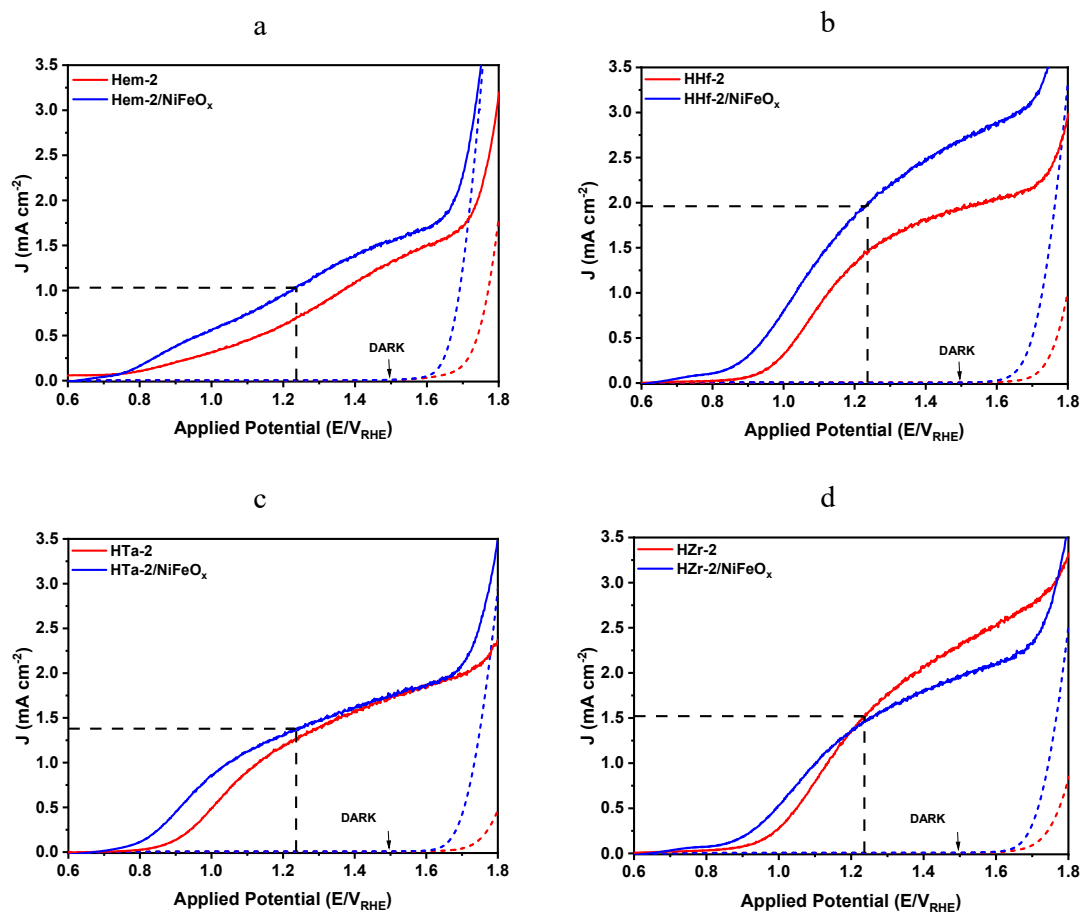
**Figure 17 – Linear sweep voltammetry analysis for spin coating optimization for Ta<sup>5+</sup> addition under light calibrated at 100 mW cm<sup>-2</sup> and dark conditions in NaOH (1.0 M) aqueous solution.**

Figure 18 shows the spin coating optimization for Zr<sup>4+</sup> addition, where the samples are named HZr-5s, HZr-10s, and HZr-20s. First looking at the onset potential, a shift is observed in the modified samples compared to the pristine hematite. In the case of Zr<sup>4+</sup> additions, the HZr-20s has the higher photocurrent, where the obtained photocurrent density were 0.75, 1.61, 1.54, and 1.81 mA cm<sup>-2</sup> for Hem, HZr-5s, HZr-10s, and HZr-20s, respectively.



**Figure 18 – Linear sweep voltammetry analysis for spin coating optimization for  $Zr^{4+}$  addition.**

In order to passivate the surfaces states created after element addition by spin coating, a cocatalyst was deposited on the film surface, as detailed in section 4.5, specifically on the films that present a higher positive shift in the onset potential such as HHf, HTa, and HZr prepared by spin coating conditions of 500 rpm for 10 seconds. This condition was chosen due to the hypothesis that the cocatalyst could shift the onset potential for lowers potentials, as shown in Figure 3 in a dotted grey line by increasing the transfer rate or by acting as a passivating agent. Figure 19 a, b, c, and d show the photocurrent response with (Hem-2/NiFeO<sub>x</sub>, HHf-2/NiFeO<sub>x</sub>, HTa-2/NiFeO<sub>x</sub>, and HZr-2/NiFeO<sub>x</sub>, respectively) and without (Hem-2, HHf-2, HTa-2, and HZr-2, respectively) the cocatalyst incorporation. For Hem-2/NiFeO<sub>x</sub>, HHf-2/NiFeO<sub>x</sub> the shape of the LSV suggests that NiFeO<sub>x</sub> acts as a passivating agent, whereas for HTa-2/NiFeO<sub>x</sub> and HZr-2/NiFeO<sub>x</sub> the NiFeO<sub>x</sub> can be acting as a cocatalyst since only the onset potential shifted. The photocurrent density for Hem-2/NiFeO<sub>x</sub>, HHf-2/NiFeO<sub>x</sub>, HTa-2/NiFeO<sub>x</sub>, and HZr-2/NiFeO<sub>x</sub> were 1.01, 1.96, 1.35, and 1.45 mA cm<sup>-2</sup>, respectively, where only for the HZr-2/NiFeO<sub>x</sub> there is no improvement of the photocurrent response.



**Figure 19 - Study of photoelectrodeposition cocatalyst on the pristine hematite and hematite-modified films. The LSV was measured under light calibrated at  $100 \text{ mW cm}^{-2}$  and dark conditions in NaOH (1.0 M) aqueous solution.**

The intrinsic properties were investigated by electrochemical impedance spectroscopy (EIS) in darkness, where the Mott-Schottky (M-S) analysis is shown in Figure 20 at a frequency of 1 kHz, which is high enough for the model [131]. According to Eq. (10), the donor density carrier ( $N_D$ ) is obtained by the slope where plot  $1/C^2$  versus applied potential. The  $N_D$  were  $4.54 \times 10^{19}$ ,  $3.24 \times 10^{19}$ ,  $3.18 \times 10^{19}$ , and  $2.44 \times 10^{19} \text{ cm}^{-3}$  for Hem, HHf, HTa, and HZr, respectively. These values indicate that any element is being inserted on the hematite network since they have the same magnitude order.

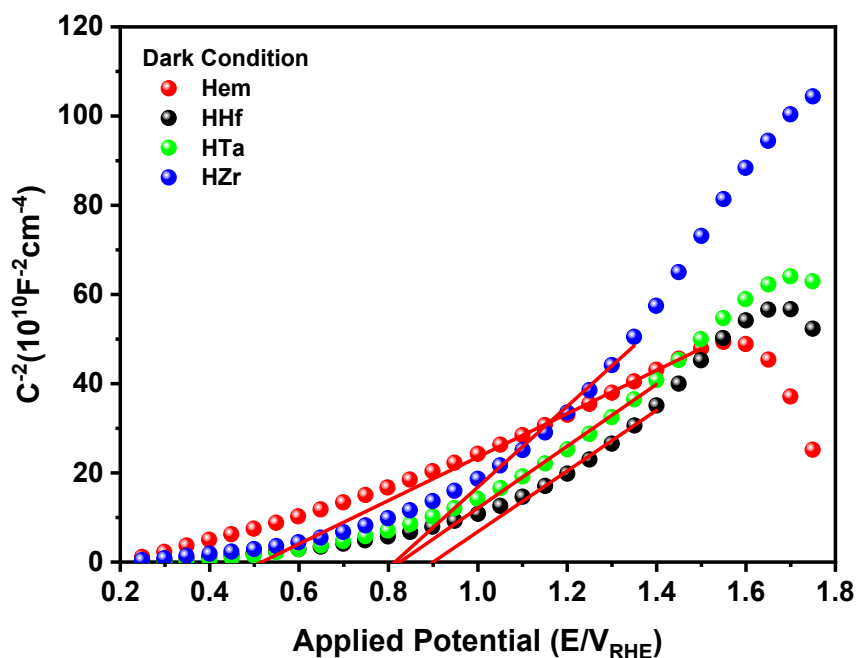
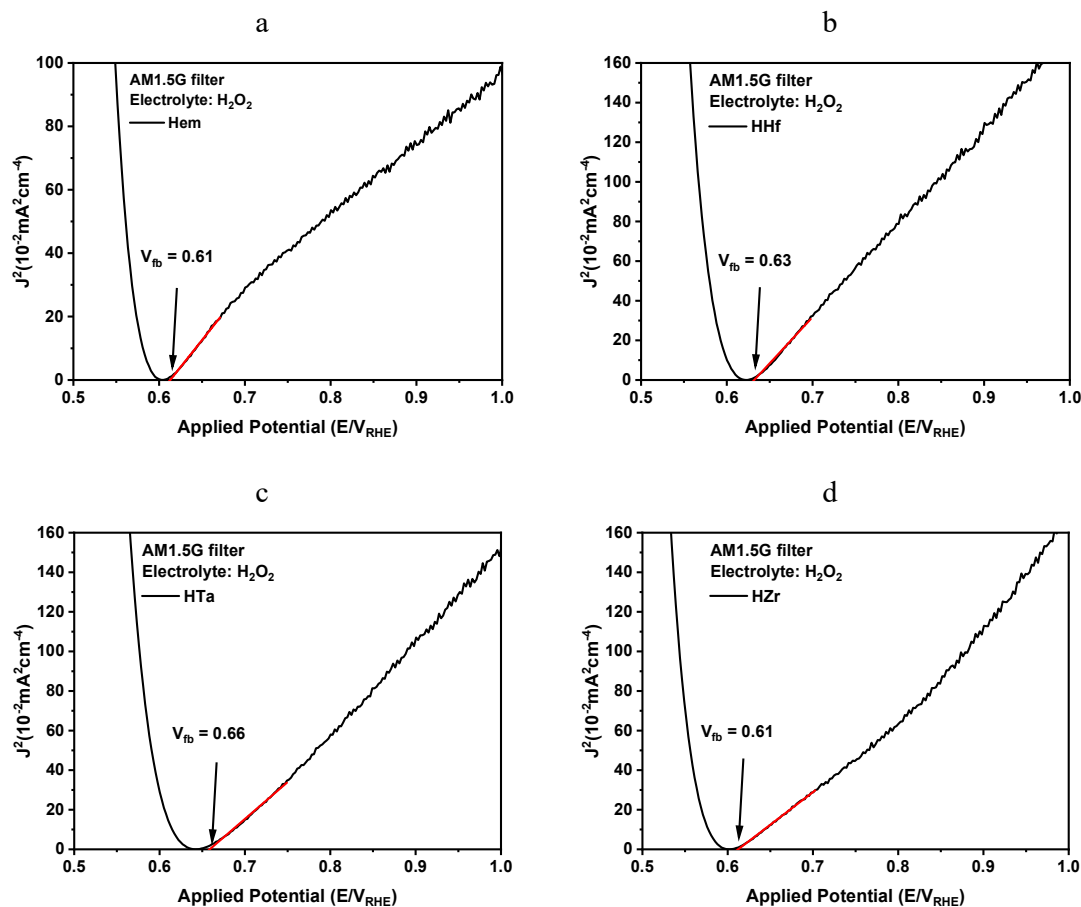


Figure 20 – Mott-Schottky analysis in darkness at 1kHz for Hem, HHf, HTa, and HZr samples.

The flatband potential ( $V_{\text{fb}}$ ) was obtained via Gärtner-Butler analysis [126] as detailed in section 4.3 since the M-S analysis gives a deviation from similar materials [132]. To obtain the  $V_{\text{fb}}$ , the LSV was performed with an addition of 5% of  $\text{H}_2\text{O}_2$  in the electrolyte, where the  $\text{H}_2\text{O}_2$  acts as a hole scavenger. By plotting the  $J_{\text{ph}}^2$  versus applied potential and extrapolating the linear part of the curve, as shown in Figure 21, the  $V_{\text{fb}}$  is given by the intersection of the x-axis. The obtained  $V_{\text{fb}}$  were 0.61, 0.63, 0.66, and 0.61 for Hem, HHf, HTa, and HZr, respectively. And the space charge layer was estimated using the Eq. (8), which is 17, 21, 21, and 23 nm for Hem, HHf, HTa, and HZr respectively, where a slight increase can be observed for the hematite-modified samples. As observed, any significant change in  $V_{\text{fb}}$  is obtained after element modification. Indeed, the space charge layer slightly increase, suggesting that the photocurrent enhancement is directly related to an enhancement in the charge separation efficiency provoked by the internal electric field through the nanorod.



**Figure 21 - Flatband potential determination for a) Hem, b) HHf, c) HTa, and d) HZr.**

The X-ray diffraction analysis was used to confirm that only the hematite phase was obtained. Figure 22 shows the patterns for Hem, HHf, HTa, and HZr, in which the hematite phase was indexed according to the JCPDS card 033-0664, confirming the formation of the hematite phase. Additional diffraction peaks associated with  $Hf^{4+}$  and  $Ta^{5+}$  addition were not detected, except for FTO peaks as indicated with an asterisk, and for HZr the  $ZrO_2$  was indexed with the card JCPDS-034-1084, confirming the formation of a second phase. In this way, the work was continued by using the  $Hf^{4+}$  as a modifier, which has a higher photocurrent response.



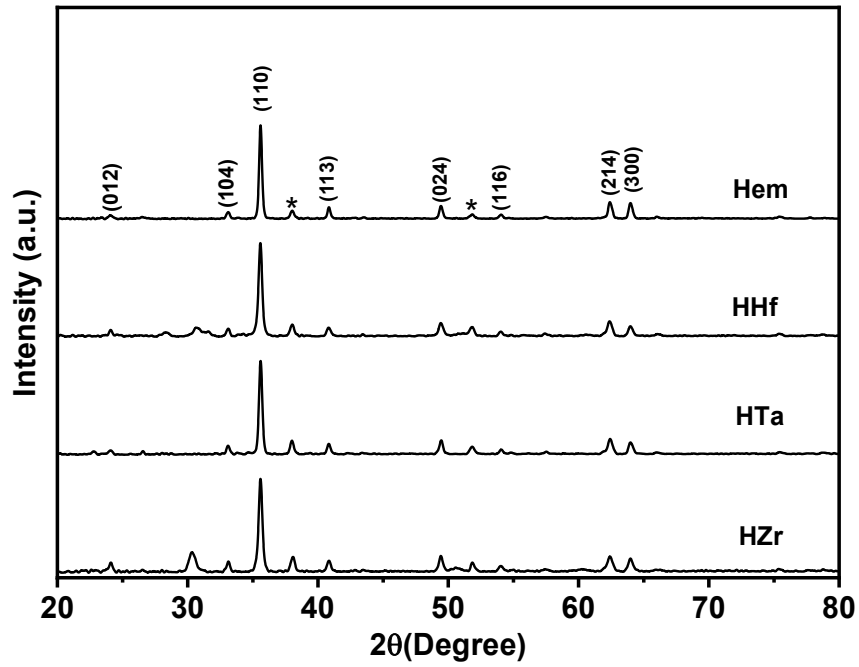
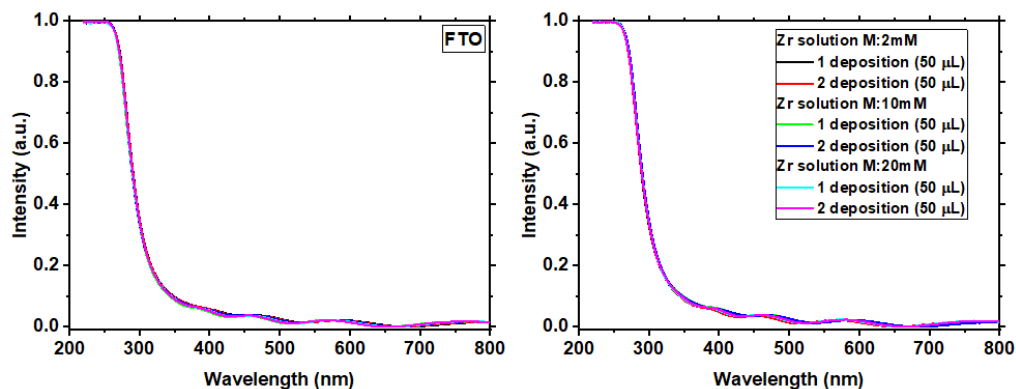


Figure 22 - X-ray diffraction patterns for Hem, HHf, HTa, and HZr.

### 5.3. Blocking layer

To mitigate the electron loss collected at the back contact (FTO) to the electrolyte, a blocking layer (BL) was coated on the cleaned FTO before growing the film. It is desired that the BL cannot change any optical property of the FTO. According to Figure 23, the spectrophotometry analysis of the FTO with and without the covered BL, the spectra have the same behavior, indicating that the BL is ‘transparent’, thus, it does not interfere with the substrate optical properties.



**Figure 23 - UV-Vis measurement of the FTO with and without the blocking layer coating. On the left side, we show the UV-Vis spectra of bare FTO, and on the right side the UV-Vis spectra of the FTO covered with the blocking layer, showing that the blocking layer does not improve the light absorption.**

For this particular method of synthesis, the blocking layer must be resistant in an acid environment, in which the precursor solution has a  $\text{pH} = 1.5$ . To investigate the best element to use as a BL, the use of  $\text{Al}_2\text{O}_3$ ,  $\text{HfO}_2$ ,  $\text{Nb}_2\text{O}_5$ ,  $\text{Ta}_2\text{O}_5$ ,  $\text{TiO}_2$ , and  $\text{ZrO}_2$  was investigated. The sample was named by adding the symbol of the element and a symbol of division (/) before the previous name. Figure 24 shows the photocurrent response of each, where only the Ta/HHf and Zr/HHf showed an increase in the photocurrent response. The photocurrents were  $2.00$  and  $2.07$   $\text{mA cm}^{-2}$  for Ta/HHf and Zr/HHf respectively. There is no shift in the onset potential, which indicated that the surface states are just from  $\text{Hf}^{4+}$  incorporation.

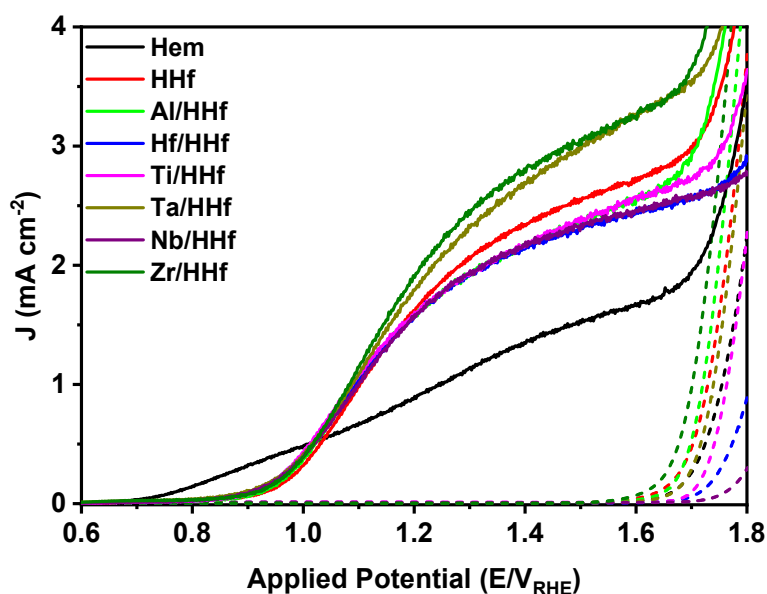


**Figure 24 - Blocking layer study with the elements:  $\text{Al}_2\text{O}_3$ ,  $\text{HfO}_2$ ,  $\text{Nb}_2\text{O}_5$ ,  $\text{Ta}_2\text{O}_5$ ,  $\text{TiO}_2$ , and  $\text{ZrO}_2$ .**

The BL-Zr spin coating was optimized by varying the concentration of the ethanoic solution (2, 10, and 20 mM), and further varying the number of depositions (1 or 2 depositions). Cyclic voltammetry (CV) was performed, where the potassium hexacyanoferrate is a transfer of an electron[133], and a current response indicates that the electron was transferred between the FTO and the electrolyte. Figure 25 a and b, show that these conditions are not efficient, where an oxidation and reduction signal is shown. While the others conditions are probably able to mitigate the electron loss.

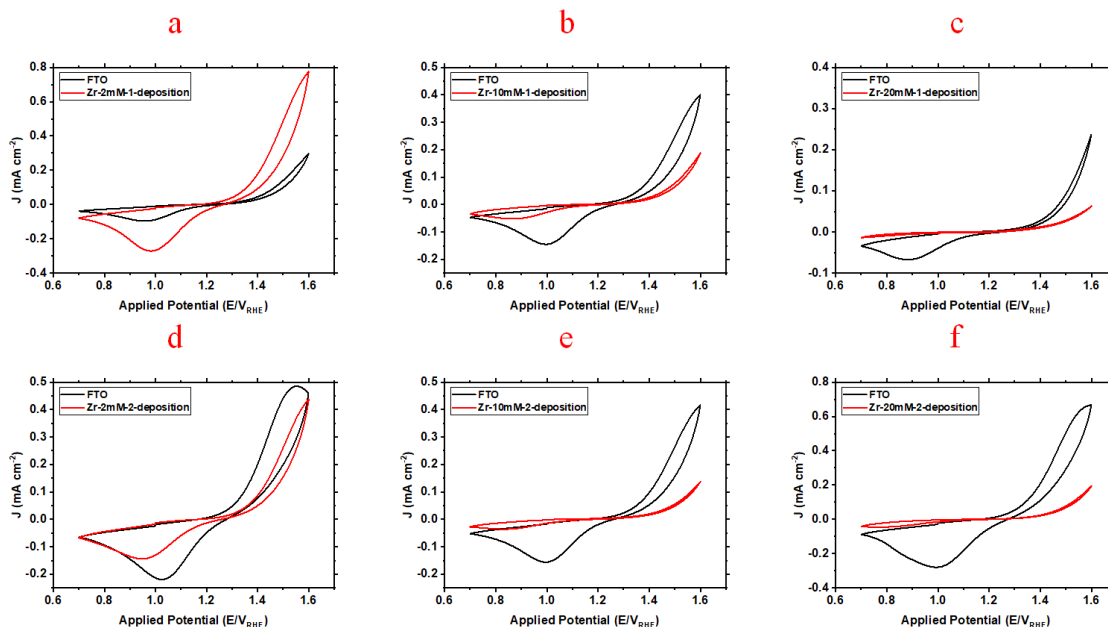


**Figure 25 - Cyclic voltammetry (CV) of blocking layer optimization. CV measurements were recorded from 0.7 to 1.6 VRHE, using a scan rate of  $10 \text{ mV s}^{-1}$  immersed in Aan electrolyte solution containing 1.0 M of KOH, and 10 mM of  $\text{K}_4[\text{Fe}(\text{CN})_6]$ .**

The above optimization was performed without synthesizing the film, where only the blocking layer was deposited. The BL conditions of 10 mM with 1 and 2 depositions and 20 mM with 1 and 2 depositions were used to synthesize a photoelectrode of modified hematite. Figure 26 shows the LSV measurement, where the highest photocurrent response was obtained with 10 mM with 1 and 2 depositions.

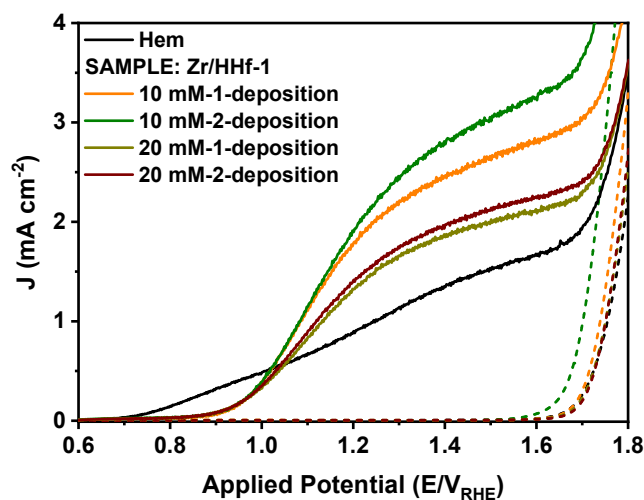


**Figure 26 - Linear sweep voltammetry of different conditions of the blocking layer design. The LSV curves were measured under light calibrated at  $100 \text{ mW cm}^{-2}$  and dark conditions in NaOH (1.0 M) as electrolyte solution.**

#### 5.4. Photoelectrodes study

All of the mentioned optimizations were important to obtain the best performance of the photoelectrodes in each step. Of course, the study was not finished, since the BL-Ta showed almost the same photocurrent response compare to BL-Zr. However, at this point, the photoelectrodes studies were pristine hematite as a standard sample, hematite with  $\text{Hf}^{4+}$  modifier (HHf) insert via spin coating (500 rpm/10s), and the hematite modified with Hf and the blocking layer of Zr (Zr/HHf).

The first investigation was the confirmation of the  $\alpha\text{-Fe}_2\text{O}_3$  phase, where the X-ray diffraction patterns (Figure 27) were indexed according to the JCPDS card 033-0664, which confirms the formation of the hematite phase. Additional diffraction peaks associated with  $\text{Hf}^{4+}$  and BL-Zr addition were not detected, except for FTO peaks as indicated with an asterisk. The calculated Lotgering factor [127], were  $f = 0.44$ ,  $0.46$ , and  $0.44$  for Hem, HHf, and Zr/HHf, respectively, revealing preferential growth at the plane (110) directions, which is induced by FTO [128]. The crystallite size estimated from the Scherrer equation [129] indicates that the  $\text{Hf}^{4+}$  acts as a crystal growth suppressor, where the obtained crystallite size are  $32 \pm 2$ ,  $26 \pm 2$ , and  $24 \pm 2$  nm for Hem, HHf, and Zr/HHf respectively. The result for Zr/HHf ( $24 \pm 2$  nm) suggests the BL-Zr does not significantly affect the crystallite size. The cell parameters were calculated as  $a = 5.03 \pm 0.001 \text{ \AA}$ ,  $c = 13.74 \pm 0.01 \text{ \AA}$ , and  $V = 301.7 \pm 0.35 \text{ \AA}^3$  for all samples, indicating Hf and Zr are not significantly dissolving in the crystalline network.

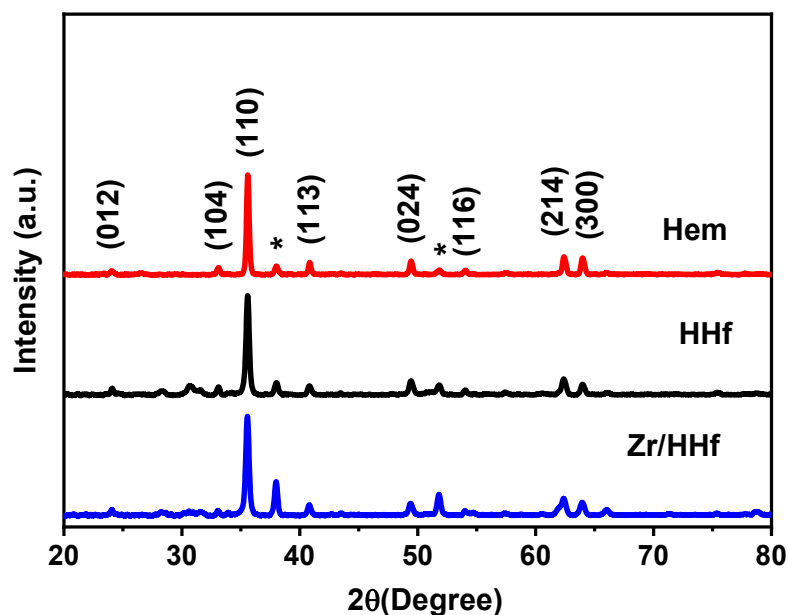


**Figure 27 - X-ray diffraction of H, HHf, and Zr/HHf samples.**

A cross-section FIB-SEM image (Figure 28 – a'', b'', and c'') revealed that all photoanodes have nanorods morphology, with the thickness of  $500 \pm 30$  nm,  $502 \pm 30$  nm, and  $537 \pm 30$  nm, with rod diameters (Figure 28 – a''', b''', and c''') of  $54 \pm 11$  nm,  $31 \pm 7$  nm, and  $30 \pm 5$  nm for Hem, HHf, and Zr/HHf, respectively. Consistent with the crystallite sizes, the rod dimensions were also impacted by Hf. The thickness variation in Zr/HHf is however related to the addition of the  $\text{ZrO}_2$  blocking layer. For all samples, Atomic Force Microscopy (AFM) (Figure 28 – a, b, and c) of the surfaces indicates the Root Mean Square (RMS) shows negligible changes ( $102 \pm 3$  nm,  $96 \pm 6$  nm, and  $101.7 \pm 2$  nm for Hem, HHf, and Zr/HHf respectively) indicating consistent surface roughnesses.

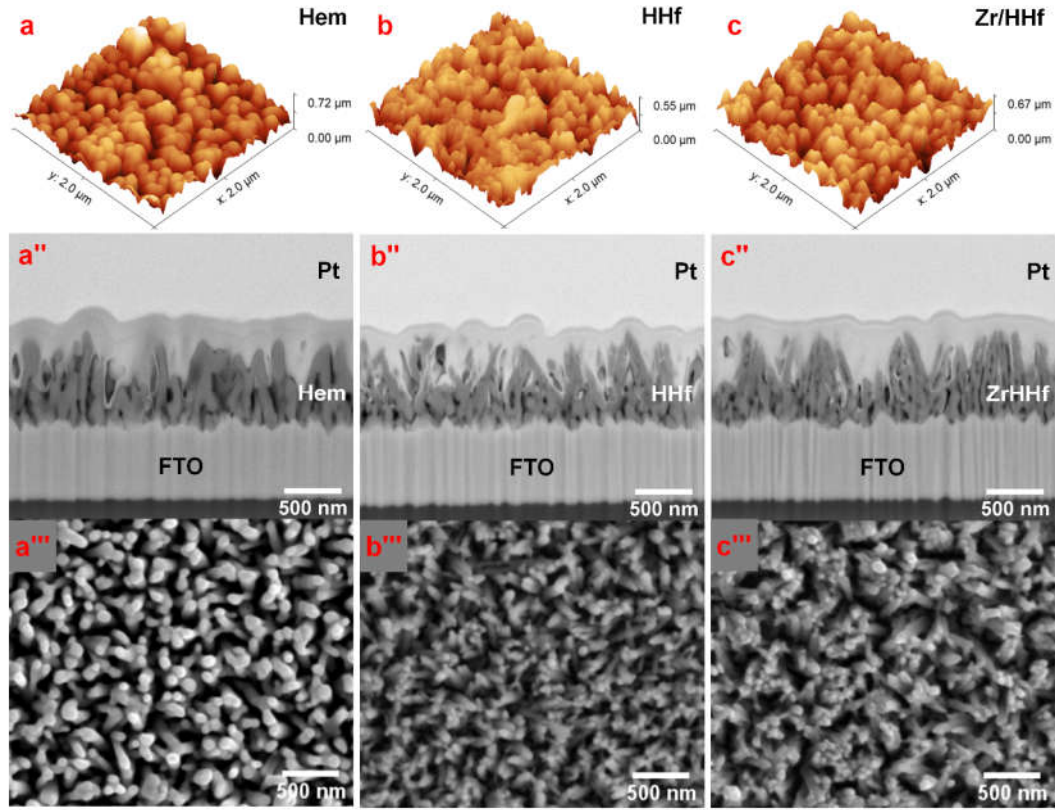


**Figure 28 - a, b, and c is the topographic image obtained from Atomic Force Microscopy of the Hem, HHf, and Zr/HHf, respectively. a'', b'', and c'' are FIB-SEM images of the cross-section view of the Hem, HHf, and Zr/HHf, respectively. a''', b''', and c''' are FIB-SEM images of the top view of the Hem, HHf, and Zr/HHf, respectively.**

The  $\text{Hf}^{4+}$  distribution on hematite was identified by semi-qualitative analysis of energy-dispersive X-ray spectroscopy (EDS). Figure 29 shows the EDS analysis, which was mapping a determined region of the sample. Bottom to up, the tin (blue) observed comes from the FTO, the iron (yellow) is related to the hematite, and the platinum is a protective layer deposited by FIB-SEM before the ion gun starts the sample degradation. The EDS identified the hafnium (red) disperse on the top of the nanorod, which is related to the method of deposition.

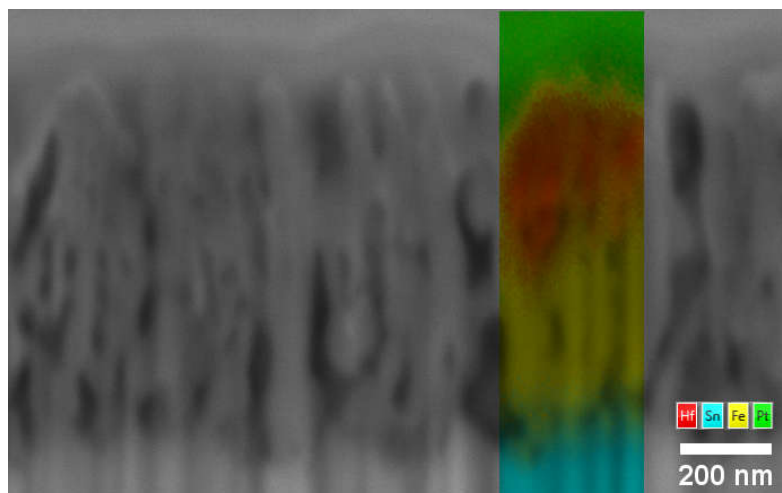


**Figure 29 - Energy-dispersive X-ray spectroscopy analysis of Zr/HHf.**

Figure 30 shows the spectrophotometry analysis of pristine hematite (Hem), hematite modified with  $\text{Hf}^{4+}$  (HHf), and HHf modified with a blocking layer of  $\text{ZrO}_2$  (Zr/HHf). The  $J_{\text{abs}}$  calculated from Eq. (9) present a slight decrease, where Hem, HHf, and Zr/HHf are  $8.8 \pm 0.2$ ,  $7.6 \pm 0.1$ , and  $8.0 \pm 0.3 \text{ mAcm}^{-2}$ , respectively.

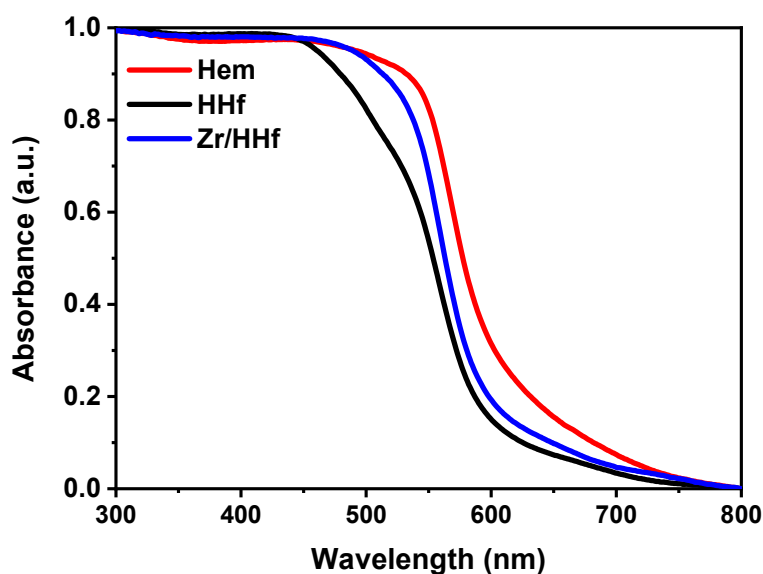


**Figure 30 - Spectrophotometry analysis of H, HHf, and Zr/HHf.**

Figure 31 shows the linear sweep voltammetry (LSV) measurements under dark and light conditions (dash and solid lines, respectively). The photocurrent density ( $J_{\text{ph}}$ ) versus applied potential (in reversible hydrogen electrode – RHE) curves show that the photocurrent response at  $1.23 \text{ V}_{\text{RHE}}$  for Hem, HHf, and Zr/HHf photoanodes are  $0.75$ ,  $1.80$ , and  $2.07 \text{ mA cm}^{-2}$ , respectively. A small photocurrent onset shift at more positive potential is observed after  $\text{Hf}^{4+}$



addition which has been associated with the creation of additional surface defects [105]. More importantly, a considerable enhancement in overall efficiency ( $\eta_{\text{overall}}$ ), determined by the ratio between  $J_{\text{ph}}$  and  $J_{\text{abs}}$ , from  $8 \pm 0.5\%$  for Hem to  $22 \pm 3.2\%$ , and  $26 \pm 0.8\%$  for HHf and Zr/HHf is observed.

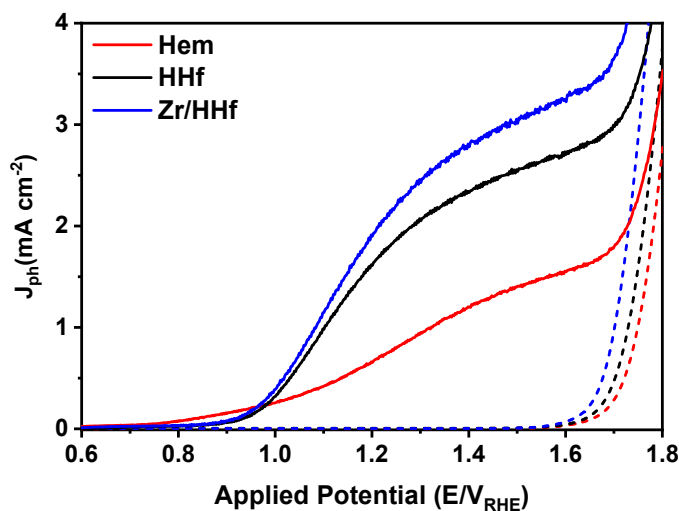


**Figure 31 - Compilation of the photocurrent curves of the investigated samples. The LSV were measured under light calibrated at  $100 \text{ mW cm}^{-2}$  and dark conditions in NaOH (1.0 M) as electrolyte solution.**

The donor density carrier ( $N_D$ ) and space charge layer ( $w$ ) were investigated by Mott-Schottky (M-S) plot (Figure 32) obtained from electrochemical impedance spectroscopy (EIS) in darkness. The obtained  $N_D$  were  $4.5 \times 10^{19}$ ,  $3.3 \times 10^{19}$ , and  $2.8 \times 10^{19} \text{ cm}^{-3}$  for Hem, HHf, and Zr/HHf, respectively.

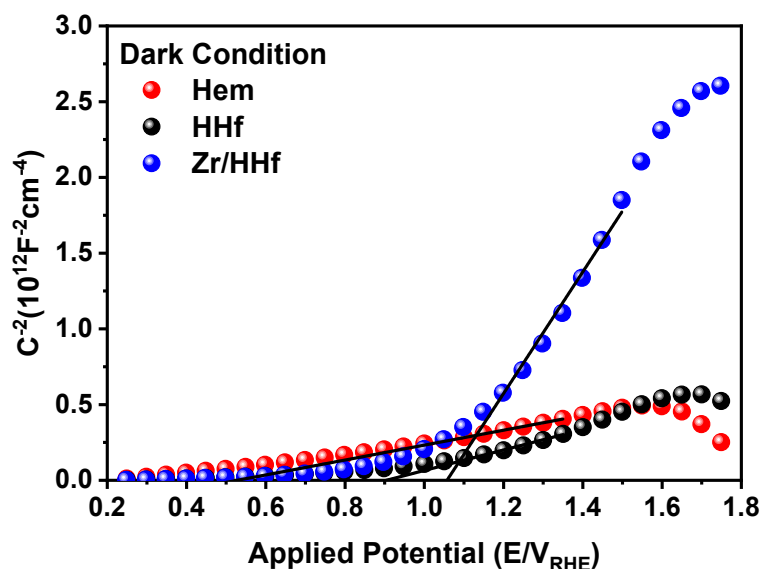


Figure 32 - Mott-Schottky plot of H, HHf, and Zr/HHf samples.

The flatband potential ( $V_{fb}$ ) estimated by Gärtner–Butler analysis [126] was 0.6 for all photoanodes, which remains constant.  $W$  obtained from Eq. (8), slightly varies (17, 21, and 22 nm for Hem, HHf, and Zr/HHf respectively). This indicates neither Hf nor  $ZrO_2$  underlayer is changing the hematite electronic properties significantly, but both are mainly modifying its charge carrier kinetics.

### 5.5. Charge carrier dynamic

The charge carrier dynamics were investigated in the pristine hematite (Hem), Hf-modified hematite (HHf), and HHf with  $ZrO_2$  blocking layer (Zr/HHf). For decades, the photocurrent versus voltage curves has been tried to be explained in terms of the charge carrier dynamics due to the difference between the theoretical and experimental photocurrent observed. Generally, steady-state characterization techniques were used due to their acceptance among the researchers. However, nonstationary techniques demonstrated an important contribution to advances in semiconductors in photoelectrochemistry. As mentioned in previous sections, the water-splitting process involves three main steps. The process starts with the generation of the charge carriers by light absorption. The electron-hole pair is generated when the incident photon has an energy higher than the bandgap. Subsequently, the electron-hole pair photogenerated can be separated where the majority carrier (electron for an n-type) moves to the back contact. The minority carrier travels to the semiconductor/electrolyte interface. However, during the process, the carrier can recombine at the surface, or the defects can trap

the charge, and the water splitting not occurs. The charge carrier that reaches the semiconductor/electrolyte interface can perform the oxygen evolution reaction.

Intensity-modulated photocurrent spectroscopy (IMPS) is a non-stationary technique to study the kinetics process of photoelectrochemical reactions at the semiconductor/electrolyte interface. IMPS was used by analyzing the external quantum efficiency ( $EQE$ ), charge separation efficiency ( $CSE$ ), surface recombination ( $k_{sr}$ ), and transfer ( $k_{tr}$ ) constants as a function of the applied potential. The Nyquist plot is composed of the real and the imaginary part of the transfer function,  $H'$  and  $H''$ . The transfer function  $H$  is given by Eq. (11).

$$H = \frac{\widetilde{J}_{ph}}{\widetilde{I}} = \frac{J_{ph}}{I} \exp(i\varphi) \quad (11)$$

where the  $\widetilde{J}_{ph}$  is the modulated photocurrent read by the analysis due to the modulated light intensity,  $\widetilde{I}$ , and  $\varphi$  is the phase shift between  $\widetilde{J}_{ph}$  and  $\widetilde{I}$ . The modulation of the light intensity is a periodic function of  $\varphi$ , and can be written as  $\omega t$  and allows us to use Euler's formula for imaginary numbers. Where the  $H$  can be written as Eq. (12).

$$H = \frac{J_{ph}}{I} \exp(i\varphi) = \text{Re}(H) + i\text{Im}(H) = H' + iH'' \quad (12)$$

From the Nyquist plot, it can be observed that the IMPS transfer function ( $H$ ) for Hem (Figure 33) is composed of a high-frequency and low-frequency loop in all potential ranges. Following the model described by McAleer and Peter in 1980 [134], the intersection of the x-axis at low frequency corresponds to the direct current (DC) external quantum efficiency ( $EQE$ ). From the 4<sup>th</sup> quadrant, the IMPS spectra start on zero for all samples, because the electrochemical system process is not able to follow high light modulation (20 kHz). The semicircle on 1<sup>st</sup> quadrant is associated with charge recombination problems due to the presence of surface states.

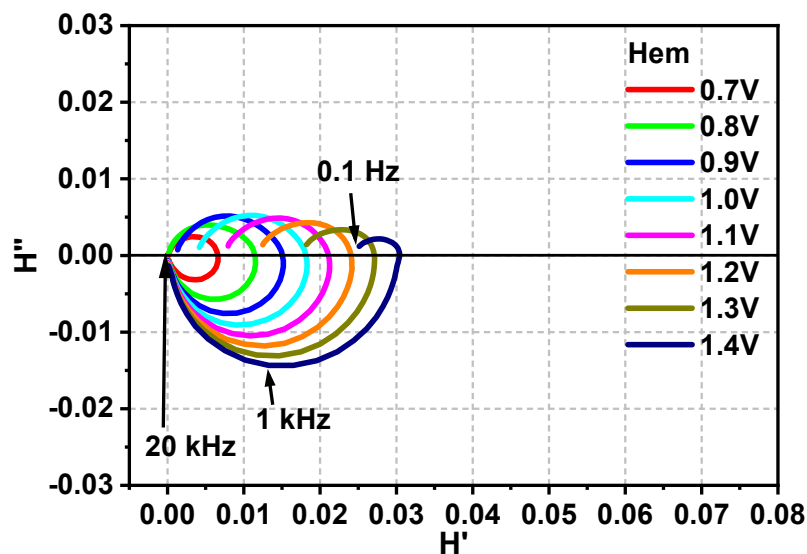


Figure 33 - Nyquist plot from IMPS analysis of Hem.

For HHf (Figure 34) the low-frequency loop disappears at  $V_{RHE} > 1.3 V_{RHE}$ .

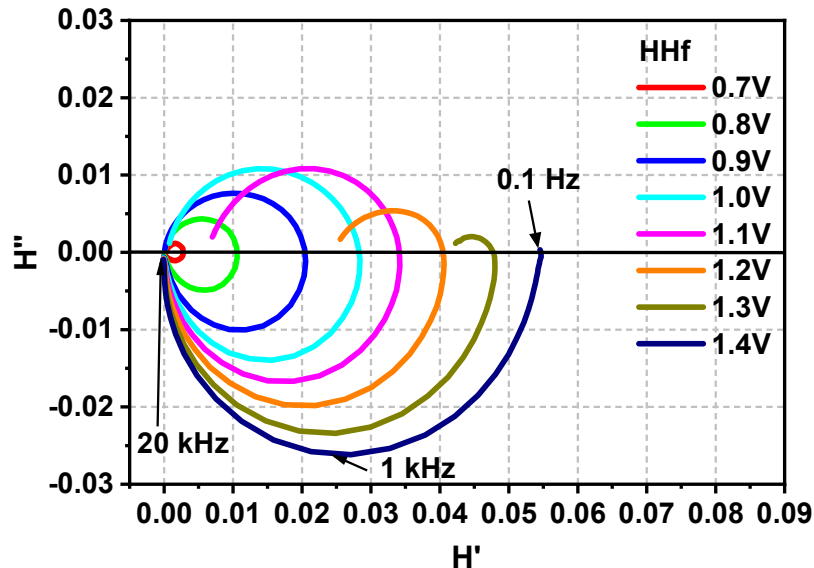


Figure 34 - Nyquist plot from IMPS analysis of HHf.

For Zr/HHf (Figure 35) the loop disappears at  $V_{RHE} > 1.2 V_{RHE}$ , indicating that the surface processes are no longer dependent on the applied potential.

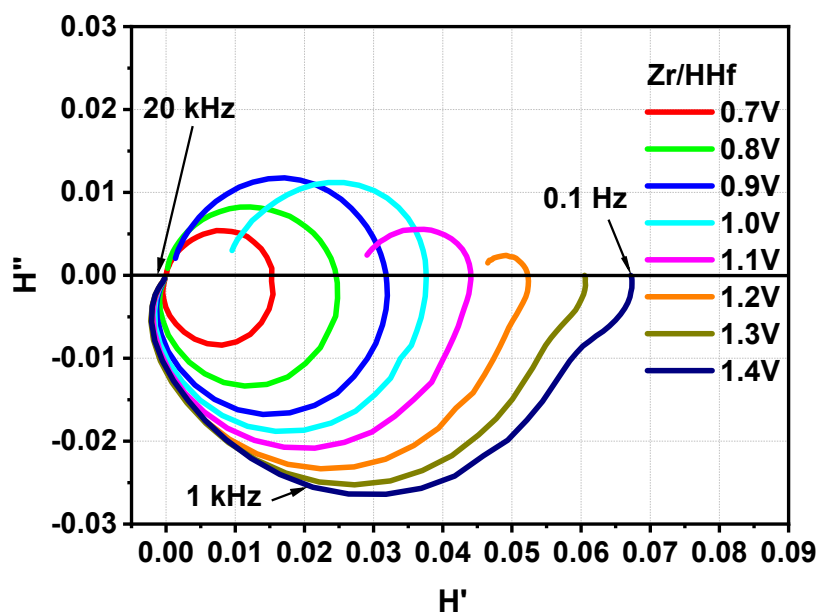


Figure 35 - Nyquist plot from IMPS analysis of Zr/HHf.

The  $k_{tr}$  deconvoluted from the IMPS spectra (Figure 36) presents a similar trend for all photoanode, indicating that the transfer constant is not altered by the Hf addition or the presence of  $ZrO_2$  underlayer. Similarly, a constant trend for  $(RC)^{-1}$  time is observed constantly.

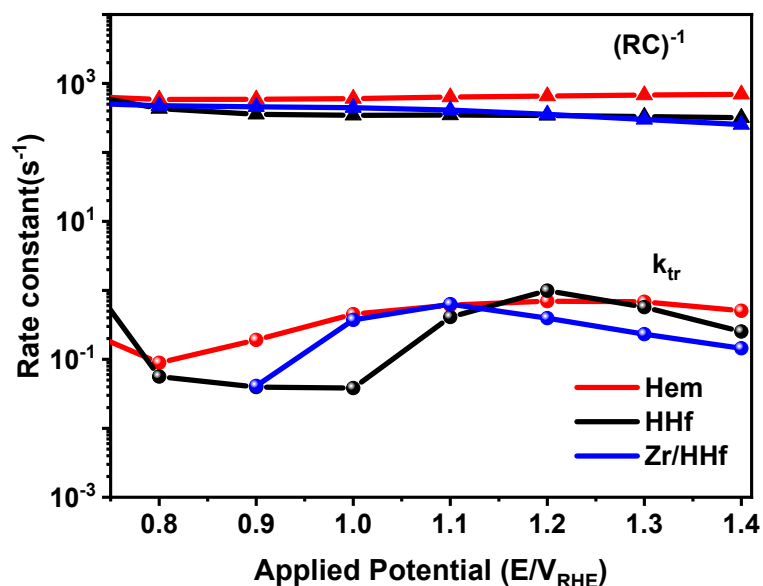


Figure 36 - Transfer and RC constants in the function of applied potentials.

However, in Figure 37, a more pronounced decrease in  $k_{rec}$  for HHf and Zr/HHf photoanodes suggests that  $Hf^{4+}$  is altering the surface processes. Interestingly, the intercept at

a medium frequency related to *CSE* is significantly greater for Zr/HHf and HHf than for Hem, confirming that  $\text{Hf}^{4+}$  and  $\text{ZrO}_2$  are mostly improving the electron collection, which justifies this enhancement in charge separation.

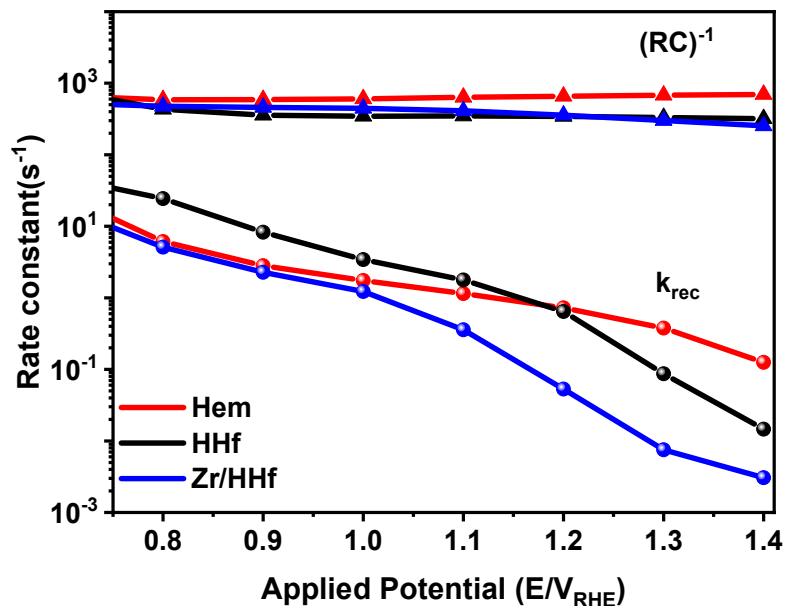


Figure 37 - Recombination and RC constants in the function of applied potentials.

Figure 38 shows the charge separation efficiency versus applied potential obtained from IMPS spectra, which confirms the previous observation

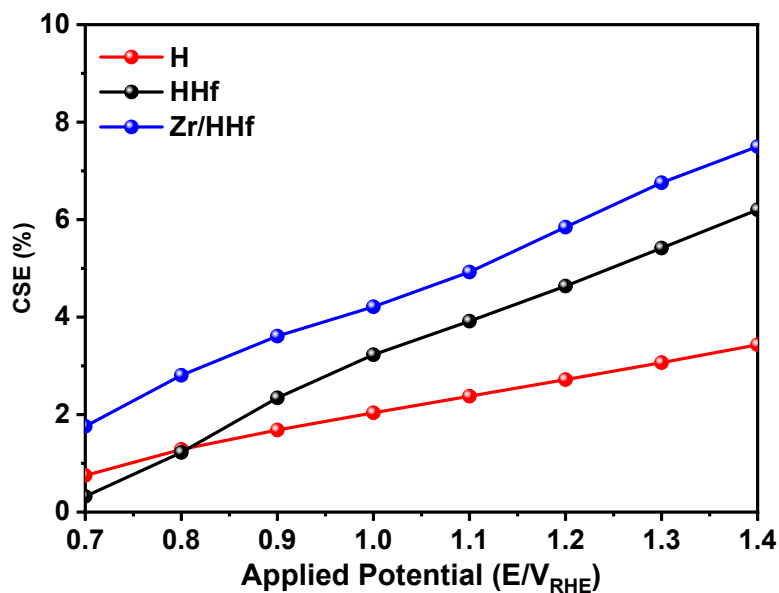


Figure 38 - Charge separation efficiency versus applied potential.

## 6. CONCLUSION

The development of technology for green hydrogen production would enable the transition towards truly sustainable societies. To achieve the commercial target value of at least 10% in solar-to-hydrogen (STH) conversion, diverse modifications during the synthesis must be performed. In the present thesis, it has been shown that well-established methodologies could potentially be improved by simply modifying some parameters such as temperature in hydrothermal synthesis. Apparently, this parameter can potentially modify the absorption properties by inducing different rod lengths and diameters. Surface modifications such as element addition or blocking layers can both enhance the charge separation by acting in different ways. For element incorporation, charge separation can be enhanced due to the creation of an internal electric field. The blocking layer avoids the possible electron losses from the substrate and minimizes the recombination at this interface.

Although all elements tested in this thesis show interesting results, the  $\text{Hf}^{4+}$  insertion shows promisors and non-fully explored results in the literature. Even though Hf addition improves the PEC performance by enhancing charge separation efficiency, the creation of additional surface states shifts the photocurrent onset at more positive potentials and affects the surface recombination rate constant. The inclusion of a  $\text{ZrO}_2$  thin underlayer helps to avoid the electron losses at the FTO back contact, thus, improving the electron collection which positively affects the charge separation efficiency. The combination of an element addition, as well as an underlayer presence, represents a rational design that leads to the improvement in the PEC performance of hematite nanorod array photoanodes for solar water splitting.

## 7. REFERENCES

- [1] R. D. K. Misra, A. Kale, R. S. Srivastava, and O. N. Senkov, "Synthesis of nanocrystalline nickel and zinc ferrites by microemulsion technique," *Mater. Sci. Technol.*, vol. 19, no. 6, pp. 826–830, Jun. 2003.
- [2] P. . Edwards, V. . Kuznetsov, and W. I. . David, "Hydrogen energy," *Philos. Trans. R. Soc. A Math. Phys. Eng. Sci.*, vol. 365, no. 1853, pp. 1043–1056, Apr. 2007.
- [3] A. Züttel, A. Remhof, A. Borgschulte, and O. Friedrichs, "Hydrogen: the future energy carrier," *Philos. Trans. R. Soc. A Math. Phys. Eng. Sci.*, vol. 368, no. 1923, pp. 3329–3342, Jul. 2010.
- [4] N. P. Brandon and Z. Kurban, "Clean energy and the hydrogen economy," *Philos. Trans. R. Soc. A Math. Phys. Eng. Sci.*, vol. 375, no. 2098, p. 20160400, Jul. 2017.
- [5] J. O. Abe, A. P. I. Popoola, E. Ajenifuja, and O. M. Popoola, "Hydrogen energy, economy and storage: Review and recommendation," *Int. J. Hydrogen Energy*, vol. 44, no. 29, pp. 15072–15086, Jun. 2019.
- [6] K. Espegren, S. Damman, P. Piscicella, I. Graabak, and A. Tomasgard, "The role of hydrogen in the transition from a petroleum economy to a low-carbon society," *Int. J. Hydrogen Energy*, vol. 46, no. 45, pp. 23125–23138, Jul. 2021.
- [7] P. M. Falcone, M. Hiete, and A. Sapio, "Hydrogen economy and sustainable development goals: Review and policy insights," *Curr. Opin. Green Sustain. Chem.*, vol. 31, p. 100506, Oct. 2021.
- [8] B. C. Tashie-Lewis and S. G. Nnabuife, "Hydrogen Production, Distribution, Storage and Power Conversion in a Hydrogen Economy - A Technology Review," *Chem. Eng. J. Adv.*, vol. 8, no. March, p. 100172, Nov. 2021.
- [9] J. Ohi, "Hydrogen energy cycle: An overview," *J. Mater. Res.*, vol. 20, no. 12, pp. 3180–3187, Dec. 2005.
- [10] T. I. Sigfusson, "Pathways to hydrogen as an energy carrier," *Philos. Trans. R. Soc. A Math. Phys. Eng. Sci.*, vol. 365, no. 1853, pp. 1025–1042, Apr. 2007.
- [11] Z. Abdin, A. Zafaranloo, A. Rafiee, W. Mérida, W. Lipiński, and K. R. Khalilpour, "Hydrogen as an energy vector," *Renew. Sustain. Energy Rev.*, vol. 120, no. November 2019, p. 109620, Mar. 2020.
- [12] J. Michalski *et al.*, "Hydrogen generation by electrolysis and storage in salt caverns:



- Potentials, economics and systems aspects with regard to the German energy transition,” *Int. J. Hydrogen Energy*, vol. 42, no. 19, pp. 13427–13443, May 2017.
- [13] H. Nazir *et al.*, “Is the H<sub>2</sub> economy realizable in the foreseeable future? Part I: H<sub>2</sub> production methods,” *Int. J. Hydrogen Energy*, vol. 45, no. 27, pp. 13777–13788, May 2020.
- [14] Q. Chen and A. Braun, “Protons and the hydrogen economy,” *MRS Energy Sustain.*, vol. 4, no. 1, p. 14, Apr. 2017.
- [15] F. Lubbe, J. Rongé, T. Bosserez, and J. A. Martens, “Golden Hydrogen,” *Curr. Opin. Green Sustain. Chem.*, no. ii, p. 100732, Nov. 2022.
- [16] M. Saidi, M. H. Gohari, and A. T. Ramezani, “Hydrogen production from waste gasification followed by membrane filtration: a review,” *Environ. Chem. Lett.*, vol. 18, no. 5, pp. 1529–1556, Sep. 2020.
- [17] E. V. Kondratenko, G. Mul, J. Baltrusaitis, G. O. Larrazábal, and J. Pérez-Ramírez, “Status and perspectives of CO<sub>2</sub> conversion into fuels and chemicals by catalytic, photocatalytic and electrocatalytic processes,” *Energy Environ. Sci.*, vol. 6, no. 11, pp. 3112–3135, 2013.
- [18] S. E. Hosseini and M. A. Wahid, “Hydrogen production from renewable and sustainable energy resources: Promising green energy carrier for clean development,” *Renew. Sustain. Energy Rev.*, vol. 57, pp. 850–866, May 2016.
- [19] J. R. Rostrup-nielsen and T. Rostrup-nielsen, “Large-scale hydrogen production,” vol. 6, no. 4, 2002.
- [20] G. Kakoulaki, I. Kougias, N. Taylor, F. Dolci, J. Moya, and A. Jäger-Waldau, “Green hydrogen in Europe – A regional assessment: Substituting existing production with electrolysis powered by renewables,” *Energy Convers. Manag.*, vol. 228, no. October 2020, p. 113649, Jan. 2021.
- [21] M. Newborough and G. Cooley, “Developments in the global hydrogen market: The spectrum of hydrogen colours,” *Fuel Cells Bull.*, vol. 2020, no. 11, pp. 16–22, Nov. 2020.
- [22] S. Wu, N. Salmon, M. M.-J. Li, R. Bañares-Alcántara, and S. C. E. Tsang, “Energy Decarbonization via Green H<sub>2</sub> or NH<sub>3</sub> ?,” *ACS Energy Lett.*, vol. 7, no. 3, pp. 1021–1033, Mar. 2022.
- [23] A. I. Osman *et al.*, “Hydrogen production, storage, utilisation and environmental impacts: a review,” *Environ. Chem. Lett.*, vol. 20, no. 1, pp. 153–188, Feb. 2022.
- [24] M. A. Khan, I. Al-Shankiti, A. Ziani, and H. Idriss, “Demonstration of green hydrogen

- production using solar energy at 28% efficiency and evaluation of its economic viability,” *Sustain. Energy Fuels*, vol. 5, no. 4, pp. 1085–1094, 2021.
- [25] J. Armijo and C. Philibert, “Flexible production of green hydrogen and ammonia from variable solar and wind energy: Case study of Chile and Argentina,” *Int. J. Hydrogen Energy*, vol. 45, no. 3, pp. 1541–1558, Jan. 2020.
- [26] M. Ghazvini, M. Sadeghzadeh, M. H. Ahmadi, S. Moosavi, and F. Pourfayaz, “Geothermal energy use in hydrogen production: A review,” *Int. J. Energy Res.*, vol. 43, no. 14, pp. 7823–7851, Aug. 2019.
- [27] I. A. Gondal, S. A. Masood, and R. Khan, “Green hydrogen production potential for developing a hydrogen economy in Pakistan,” *Int. J. Hydrogen Energy*, vol. 43, no. 12, pp. 6011–6039, Mar. 2018.
- [28] Y. S. Montenegro Camacho, S. Bensaid, G. Piras, M. Antonini, and D. Fino, “Techno-economic analysis of green hydrogen production from biogas autothermal reforming,” *Clean Technol. Environ. Policy*, vol. 19, no. 5, pp. 1437–1447, Jul. 2017.
- [29] M. Ostadi, K. G. Paso, S. Rodriguez-Fabia, L. E. Øi, F. Manenti, and M. Hillestad, “Process Integration of Green Hydrogen: Decarbonization of Chemical Industries,” *Energies*, vol. 13, no. 18, p. 4859, Sep. 2020.
- [30] B. Iandolo, B. Wickman, I. Zorić, and A. Hellman, “The rise of hematite: origin and strategies to reduce the high onset potential for the oxygen evolution reaction,” *J. Mater. Chem. A*, vol. 3, no. 33, pp. 16896–16912, 2015.
- [31] A. Fujishima and K. Honda, “Electrochemical Photolysis of Water at a Semiconductor Electrode,” *Nature*, vol. 238, no. 5358, pp. 37–38, Jul. 1972.
- [32] Robert F. Pierret, *Advanced Semiconductor Fundamentals*, 2nd editio. Pearson, 2002.
- [33] M. W. Zhiqun Lin, Meidan Ye, *Multifunctional Photocatalytic Materials for Energy*, 1st ed. Elsevier, 2018.
- [34] R. van de Krol and M. Grätzel, *Photoelectrochemical Hydrogen Production*, vol. 102. Boston, MA: Springer US, 2012.
- [35] J. Tauc, R. Grigorovici, and A. Vancu, “Optical Properties and Electronic Structure of Amorphous Germanium,” *Phys. status solidi*, vol. 15, no. 2, pp. 627–637, 1966.
- [36] M. Grätzel, “Photoelectrochemical cells,” *Nature*, vol. 414, no. 6861, pp. 338–344, Nov. 2001.
- [37] O. Khaselev and J. A. Turner, “A Monolithic Photovoltaic-Photoelectrochemical Device

- for Hydrogen Production via Water Splitting,” *Science* (80-. ), vol. 280, no. 5362, pp. 425–427, Apr. 1998.
- [38] A. Duret and M. Grätzel, “Visible Light-Induced Water Oxidation on Mesoscopic  $\alpha$ - $\text{Fe}_2\text{O}_3$  Films Made by Ultrasonic Spray Pyrolysis,” *J. Phys. Chem. B*, vol. 109, no. 36, pp. 17184–17191, Sep. 2005.
- [39] F. L. de Souza and E. R. Leite, *Nanoenergy*. Berlin, Heidelberg: Springer Berlin Heidelberg, 2013.
- [40] M. Demirci Sankir, Nurdan; Sankir, *Photoelectrochemical Solar Cells*. Hoboken, NJ, USA: Wiley, 2018.
- [41] A. Hankin, F. E. Bedoya-Lora, C. K. Ong, J. C. Alexander, F. Petter, and G. H. Kelsall, “From millimetres to metres: the critical role of current density distributions in photoelectrochemical reactor design,” *Energy Environ. Sci.*, vol. 10, no. 1, pp. 346–360, 2017.
- [42] L. J. Minggu, W. R. Wan Daud, and M. B. Kassim, “An overview of photocells and photoreactors for photoelectrochemical water splitting,” *Int. J. Hydrogen Energy*, vol. 35, no. 11, pp. 5233–5244, Jun. 2010.
- [43] A. Tofanello, S. Shen, F. L. De Souza, and L. Vayssieres, “Strategies to improve the photoelectrochemical performance of hematite nanorod-based photoanodes,” *APL Mater.*, vol. 8, no. 4, 2020.
- [44] Y. Liu, N. Guijarro, and K. Sivula, “Understanding Surface Recombination Processes Using Intensity-Modulated Photovoltage Spectroscopy on Hematite Photoanodes for Solar Water Splitting,” *Helv. Chim. Acta*, vol. 103, no. 6, Jun. 2020.
- [45] A. N. C. Agbogu, M. P. Orji, and A. B. C. Ekwealor, “Effects of temperature on the optical properties of iron oxide ( $\text{Fe}_2\text{O}_3$ ) thin films synthesized by chemical bath deposition,” *Optik (Stuttg.)*, vol. 127, no. 20, pp. 9865–9870, Oct. 2016.
- [46] J. M. Gardner, S. Kim, P. C. Searson, and G. J. Meyer, “Electrodeposition of Nanometer-Sized Ferric Oxide Materials in Colloidal Templates for Conversion of Light to Chemical Energy,” *J. Nanomater.*, vol. 2011, pp. 1–8, 2011.
- [47] J.-H. Kim, H.-I. Yoo, and H. L. Tuller, “Electrical Properties and Phase Stability of a Zinc Ferrite,” *J. Am. Ceram. Soc.*, vol. 73, no. 2, pp. 258–262, Feb. 1990.
- [48] C. Xiangfeng, “Preparation and gas sensitivity properties of  $\text{ZnFe}_2\text{O}_4$  semiconductors,” *Sensors Actuators B Chem.*, vol. 55, no. 1, pp. 19–22, Apr. 1999.
- [49] A. Kundu, C. Upadhyay, and H. C. Verma, “Magnetic properties of a partially inverted zinc ferrite synthesized by a new coprecipitation technique using urea,” *Phys. Lett. A*,

- vol. 311, no. 4–5, pp. 410–415, May 2003.
- [50] S. Yu and G. M. Chow, “Carboxyl group ( $-\text{CO}_2\text{H}$ ) functionalized ferrimagnetic iron oxide nanoparticles for potential bio-applications,” *J. Mater. Chem.*, vol. 14, no. 18, pp. 2781–2786, 2004.
  - [51] Z. Li, X. Lai, H. Wang, D. Mao, C. Xing, and D. Wang, “General Synthesis of Homogeneous Hollow Core–Shell Ferrite Microspheres,” *J. Phys. Chem. C*, vol. 113, no. 7, pp. 2792–2797, Feb. 2009.
  - [52] X. Yao, J. Kong, C. Zhao, D. Zhou, R. Zhou, and X. Lu, “Zinc ferrite nanorods coated with polydopamine-derived carbon for high-rate lithium ion batteries,” *Electrochim. Acta*, vol. 146, pp. 464–471, Nov. 2014.
  - [53] Y. Behra and N. B. Singh, “Solid state properties of zinc ferrite in presence of dopants,” *Mater. Today Proc.*, vol. 5, no. 7, pp. 15451–15457, 2018.
  - [54] S. O. Aisida, P. A. Akpa, I. Ahmad, M. Maaza, and F. I. Ezema, “Influence of PVA, PVP and PEG doping on the optical, structural, morphological and magnetic properties of zinc ferrite nanoparticles produced by thermal method,” *Phys. B Condens. Matter*, vol. 571, no. May, pp. 130–136, Oct. 2019.
  - [55] K. Sathiyamurthy, C. Rajeevgandhi, S. Bharanidharan, P. Sugumar, and S. Subashchandrabose, “Electrochemical and Magnetic Properties of Zinc Ferrite Nanoparticles through Chemical Co-Precipitation Method,” *Chem. Data Collect.*, vol. 28, p. 100477, Aug. 2020.
  - [56] B. Xu *et al.*, “Simple and effective synthesis of zinc ferrite nanoparticle immobilized by reduced graphene oxide as anode for lithium-ion batteries,” *J. Colloid Interface Sci.*, vol. 584, pp. 827–837, Feb. 2021.
  - [57] R. Q. Bao, Y. R. Zhang, Z. L. Wang, Y. Liu, L. R. Hou, and C. Z. Yuan, “Core-shell N-doped carbon coated zinc ferrite nanofibers with enhanced Li-storage behaviors: A promising anode for Li-ion batteries,” *Mater. Lett.*, vol. 224, pp. 89–91, Aug. 2018.
  - [58] P. F. Teh, Y. Sharma, S. S. Pramana, and M. Srinivasan, “Nanoweb anodes composed of one-dimensional, high aspect ratio, size tunable electrospun  $\text{ZnFe}_2\text{O}_4$  nanofibers for lithium ion batteries,” *J. Mater. Chem.*, vol. 21, no. 38, p. 14999, 2011.
  - [59] H. Qiao *et al.*, “Electrospinning combined with hydrothermal synthesis and lithium storage properties of  $\text{ZnFe}_2\text{O}_4$ -graphene composite nanofibers,” *Ceram. Int.*, vol. 43, no. 2, pp. 2136–2142, Feb. 2017.
  - [60] M. Sivakumar *et al.*, “Fabrication of Zinc Ferrite Nanocrystals by Sonochemical

- Emulsification and Evaporation: Observation of Magnetization and Its Relaxation at Low Temperature,” *J. Phys. Chem. B*, vol. 110, no. 31, pp. 15234–15243, Aug. 2006.
- [61] H. Zhu, X. Gu, D. Zuo, Z. Wang, N. Wang, and K. Yao, “Microemulsion-based synthesis of porous zinc ferrite nanorods and its application in a room-temperature ethanol sensor,” *Nanotechnology*, vol. 19, no. 40, p. 405503, Oct. 2008.
- [62] R. N. Goyal, D. Kaur, and A. K. Pandey, “Growth and characterization of iron oxide nanocrystalline thin films via low-cost ultrasonic spray pyrolysis,” *Mater. Chem. Phys.*, vol. 116, no. 2–3, pp. 638–644, Aug. 2009.
- [63] J. D. Desai, H. M. Pathan, S.-K. Min, K.-D. Jung, and O.-S. Joo, “Preparation and characterization of iron oxide thin films by spray pyrolysis using methanolic and ethanolic solutions,” *Appl. Surf. Sci.*, vol. 252, no. 6, pp. 2251–2258, Jan. 2006.
- [64] A. Akbar, S. Riaz, R. Ashraf, and S. Naseem, “Magnetic and Magnetization Properties of Co-Doped  $\text{Fe}_2\text{O}_3$  Thin Films,” *IEEE Trans. Magn.*, vol. 50, no. 8, pp. 1–4, Aug. 2014.
- [65] A. Akbar, M. Imran, S. Riaz, and S. Naseem, “Study of Phase Transition in Iron Oxide Thin Films,” *Mater. Today Proc.*, vol. 2, no. 10, pp. 5405–5409, 2015.
- [66] F. L. Souza, K. P. Lopes, E. Longo, and E. R. Leite, “The influence of the film thickness of nanostructured  $\alpha\text{-Fe}_2\text{O}_3$  on water photooxidation,” *Phys. Chem. Chem. Phys.*, vol. 11, no. 8, p. 1215, 2009.
- [67] F. L. Souza, K. P. Lopes, P. A. P. Nascente, and E. R. Leite, “Nanostructured hematite thin films produced by spin-coating deposition solution: Application in water splitting,” *Sol. Energy Mater. Sol. Cells*, vol. 93, no. 3, pp. 362–368, Mar. 2009.
- [68] M. Rooth, A. Johansson, K. Kukli, J. Aarik, M. Boman, and A. Hårsta, “Atomic Layer Deposition of Iron Oxide Thin Films and Nanotubes using Ferrocene and Oxygen as Precursors,” *Chem. Vap. Depos.*, vol. 14, no. 3–4, pp. 67–70, Apr. 2008.
- [69] J. R. Avila, D. W. Kim, M. Rimoldi, O. K. Farha, and J. T. Hupp, “Fabrication of Thin Films of  $\alpha\text{-Fe}_2\text{O}_3$  via Atomic Layer Deposition Using Iron Bisamidinate and Water under Mild Growth Conditions,” *ACS Appl. Mater. Interfaces*, vol. 7, no. 30, pp. 16138–16142, Aug. 2015.
- [70] N. M. Ito, W. M. Carvalho, D. N. F. Muche, R. H. R. Castro, G. M. Dalpian, and F. L. Souza, “High temperature activation of hematite nanorods for sunlight driven water oxidation reaction,” *Phys. Chem. Chem. Phys.*, vol. 19, no. 36, pp. 25025–25032, 2017.
- [71] S. Park, S. Lim, and H. Choi, “Chemical Vapor Deposition of Iron and Iron Oxide Thin Films from  $\text{Fe(II)}$  Dihydride Complexes,” *Chem. Mater.*, vol. 18, no. 22, pp. 5150–5152,

Oct. 2006.

- [72] S.-H. Yu, T. Fujino, and M. Yoshimura, “Hydrothermal synthesis of  $\text{ZnFe}_2\text{O}_4$  ultrafine particles with high magnetization,” *J. Magn. Magn. Mater.*, vol. 256, no. 1–3, pp. 420–424, Jan. 2003.
- [73] D. Stadler *et al.*, “Magnetic Field-Assisted Chemical Vapor Deposition of Iron Oxide Thin Films: Influence of Field–Matter Interactions on Phase Composition and Morphology,” *J. Phys. Chem. Lett.*, vol. 10, no. 20, pp. 6253–6259, Oct. 2019.
- [74] J. You, X. Chen, B. Zheng, X. Geng, and C. Zhang, “Suspension Plasma-Sprayed  $\text{ZnFe}_2\text{O}_4$  Nanostructured Coatings for ppm-Level Acetone Detection,” *J. Therm. Spray Technol.*, vol. 26, no. 4, pp. 728–734, Apr. 2017.
- [75] G. Li *et al.*, “Annealing Effects on Semitransparent and Ferromagnetic  $\text{ZnFe}_2\text{O}_4$  Nanostructured Films by Sol-Gel,” *J. Am. Ceram. Soc.*, vol. 94, no. 9, pp. 2872–2877, Sep. 2011.
- [76] A. Sutka, G. Mezinskis, A. Lasis, and D. Jakovlevs, “Influence of iron non-stoichiometry on spinel zinc ferrite gas sensing properties,” *Sensors Actuators B Chem.*, vol. 171–172, pp. 204–209, Aug. 2012.
- [77] S. Singh, A. Singh, R. R. Yadav, and P. Tandon, “Growth of zinc ferrite aligned nanorods for liquefied petroleum gas sensing,” *Mater. Lett.*, vol. 131, pp. 31–34, Sep. 2014.
- [78] A. Singh, A. Singh, S. Singh, P. Tandon, B. C. Yadav, and R. R. Yadav, “Synthesis, characterization and performance of zinc ferrite nanorods for room temperature sensing applications,” *J. Alloys Compd.*, vol. 618, pp. 475–483, Jan. 2015.
- [79] D. Feng, H. Yang, and X. Guo, “3-Dimensional hierarchically porous  $\text{ZnFe}_2\text{O}_4/\text{C}$  composites with stable performance as anode materials for Li-ion batteries,” *Chem. Eng. J.*, vol. 355, no. July 2018, pp. 687–696, Jan. 2019.
- [80] R. M. Borade, S. B. Somvanshi, S. B. Kale, R. P. Pawar, and K. M. Jadhav, “Spinel zinc ferrite nanoparticles: an active nanocatalyst for microwave irradiated solvent free synthesis of chalcones,” *Mater. Res. Express*, vol. 7, no. 1, p. 016116, Jan. 2020.
- [81] S. Chakrabarty, S. Bandyopadhyay, M. Pal, and A. Dutta, “Sol-gel derived cobalt containing Ni–Zn ferrite nanoparticles: Dielectric relaxation and enhanced magnetic property study,” *Mater. Chem. Phys.*, vol. 259, no. November 2019, p. 124193, Feb. 2021.
- [82] A. Yan, X. Liu, R. Yi, R. Shi, N. Zhang, and G. Qiu, “Selective Synthesis and Properties of Monodisperse Zn Ferrite Hollow Nanospheres and Nanosheets,” *J. Phys. Chem. C*,

- vol. 112, no. 23, pp. 8558–8563, Jun. 2008.
- [83] X. Li, Y. Hou, Q. Zhao, and L. Wang, “A general, one-step and template-free synthesis of sphere-like zinc ferrite nanostructures with enhanced photocatalytic activity for dye degradation,” *J. Colloid Interface Sci.*, vol. 358, no. 1, pp. 102–108, 2011.
  - [84] Y. Li *et al.*, “Double-protected zinc ferrite nanospheres as high rate and stable anode materials for lithium ion batteries,” *J. Power Sources*, vol. 442, no. October, p. 227256, Dec. 2019.
  - [85] N. Beermann, L. Vayssieres, S.-E. Lindquist, and A. Hagfeldt, “Photoelectrochemical Studies of Oriented Nanorod Thin Films of Hematite,” *J. Electrochem. Soc.*, vol. 147, no. 7, p. 2456, 2000.
  - [86] E. . Deliyanni, D. . Bakoyannakis, A. . Zouboulis, K. . Matis, and L. Nalbandian, “Akaganéite-type  $\beta$ -FeO(OH) nanocrystals: preparation and characterization,” *Microporous Mesoporous Mater.*, vol. 42, no. 1, pp. 49–57, Jan. 2001.
  - [87] L. Vayssieres, N. Beermann, S.-E. Lindquist, and A. Hagfeldt, “Controlled Aqueous Chemical Growth of Oriented Three-Dimensional Crystalline Nanorod Arrays: Application to Iron(III) Oxides,” *Chem. Mater.*, vol. 13, no. 2, pp. 233–235, Feb. 2001.
  - [88] X. Hu, P. Guan, and X. Yan, “Hydrothermal synthesis of nano-meter microporous zinc ferrite,” *China Particuology*, vol. 2, no. 3, pp. 135–137, Jun. 2004.
  - [89] D. K. Bora, A. Braun, R. Erni, G. Fortunato, T. Graule, and E. C. Constable, “Hydrothermal treatment of a hematite film leads to highly oriented faceted nanostructures with enhanced photocurrents,” *Chem. Mater.*, vol. 23, no. 8, pp. 2051–2061, 2011.
  - [90] A. Tofanello, A. L. M. Freitas, W. M. Carvalho, T. Salminen, T. Niemi, and F. L. Souza, “Hematite Surface Modification toward Efficient Sunlight-Driven Water Splitting Activity: The Role of Gold Nanoparticle Addition,” *J. Phys. Chem. C*, vol. 124, no. 11, pp. 6171–6179, Mar. 2020.
  - [91] T. Lopes, P. Dias, L. Andrade, and A. Mendes, “An innovative photoelectrochemical lab device for solar water splitting,” *Sol. Energy Mater. Sol. Cells*, vol. 128, pp. 399–410, Sep. 2014.
  - [92] R. M. Cornell and U. Schwertmann, *The Iron Oxides*. Weinheim, Germany: Wiley, 2003.
  - [93] U. Bjoerksten, J. Moser, and M. Graetzel, “Photoelectrochemical Studies on Nanocrystalline Hematite Films,” *Chem. Mater.*, vol. 6, no. 6, pp. 858–863, Jun. 1994.
  - [94] A. Kay, I. Cesar, and M. Grätzel, “New Benchmark for Water Photooxidation by

- Nanostructured  $\alpha$ -Fe<sub>2</sub>O<sub>3</sub> Films,” *J. Am. Chem. Soc.*, vol. 128, no. 49, pp. 15714–15721, Dec. 2006.
- [95] A. B. Murphy *et al.*, “Efficiency of solar water splitting using semiconductor electrodes,” *Int. J. Hydrogen Energy*, vol. 31, no. 14, pp. 1999–2017, Nov. 2006.
- [96] J. Brillet *et al.*, “Highly efficient water splitting by a dual-absorber tandem cell,” *Nat. Photonics*, vol. 6, no. 12, pp. 824–828, Dec. 2012.
- [97] M. Orlandi *et al.*, “Rational Design Combining Morphology and Charge-Dynamic for Hematite/Nickel–Iron Oxide Thin-Layer Photoanodes: Insights into the Role of the Absorber/Catalyst Junction,” *ACS Appl. Mater. Interfaces*, vol. 11, no. 51, pp. 48002–48012, Dec. 2019.
- [98] S. R. Pendlebury *et al.*, “Ultrafast charge carrier recombination and trapping in hematite photoanodes under applied bias,” *J. Am. Chem. Soc.*, vol. 136, no. 28, pp. 9854–9857, 2014.
- [99] F. J. Morin, “Electrical Properties of  $\alpha$ -Fe<sub>2</sub>O<sub>3</sub> and  $\alpha$ -Fe<sub>2</sub>O<sub>3</sub> Containing Titanium,” *Phys. Rev.*, vol. 83, no. 5, pp. 1005–1010, Sep. 1951.
- [100] J. B. Souza Junior, F. L. Souza, L. Vayssieres, and O. K. Varghese, “On the relevance of understanding and controlling the locations of dopants in hematite photoanodes for low-cost water splitting,” *Appl. Phys. Lett.*, vol. 119, no. 20, p. 200501, Nov. 2021.
- [101] A. E. Nogueira, M. R. Santos Soares, J. B. Souza Junior, C. A. Ospina Ramirez, F. L. Souza, and E. R. Leite, “Discovering a selective semimetal element to increase hematite photoanode charge separation efficiency,” *J. Mater. Chem. A*, vol. 7, no. 28, pp. 16992–16998, 2019.
- [102] O. Zandi and T. W. Hamann, “The potential versus current state of water splitting with hematite,” *Phys. Chem. Chem. Phys.*, vol. 17, no. 35, pp. 22485–22503, 2015.
- [103] Y. He, T. Hamann, and D. Wang, “Thin film photoelectrodes for solar water splitting,” *Chem. Soc. Rev.*, vol. 48, no. 7, pp. 2182–2215, 2019.
- [104] M. R. S. Soares *et al.*, “Unraveling the Role of Sn Segregation in the Electronic Transport of Polycrystalline Hematite: Raising the Electronic Conductivity by Lowering the Grain-Boundary Blocking Effect,” *Adv. Electron. Mater.*, vol. 5, no. 6, p. 1900065, Jun. 2019.
- [105] A. L. M. Freitas, D. N. F. Muche, E. R. Leite, and F. L. Souza, “Interface engineering of nanoceramic hematite photoelectrode for solar energy conversion,” *J. Am. Ceram. Soc.*, vol. 103, no. 12, pp. 6833–6846, Dec. 2020.
- [106] T. H. Jeon, G. Moon, H. Park, and W. Choi, “Ultra-efficient and durable



- photoelectrochemical water oxidation using elaborately designed hematite nanorod arrays,” *Nano Energy*, vol. 39, no. May, pp. 211–218, Sep. 2017.
- [107] C. X. Kronawitter *et al.*, “Titanium incorporation into hematite photoelectrodes: theoretical considerations and experimental observations,” *Energy Environ. Sci.*, vol. 7, no. 10, pp. 3100–3121, 2014.
- [108] I. Cesar, A. Kay, J. A. Gonzalez Martinez, and M. Grätzel, “Translucent Thin Film  $\text{Fe}_2\text{O}_3$  Photoanodes for Efficient Water Splitting by Sunlight: Nanostructure-Directing Effect of Si-Doping,” *J. Am. Chem. Soc.*, vol. 128, no. 14, pp. 4582–4583, Apr. 2006.
- [109] X. Qi *et al.*, “High-performance n-Si/ $\alpha$ - $\text{Fe}_2\text{O}_3$  core/shell nanowire array photoanode towards photoelectrochemical water splitting,” *Nanoscale*, vol. 6, no. 6, pp. 3182–3189, 2014.
- [110] D. K. Bora, “Fabrication of silicon doped hematite photoelectrode with enhanced photocurrent density via solution processing of an in-situ TEOS modified precursor,” *Mater. Sci. Semicond. Process.*, vol. 31, pp. 728–738, Mar. 2015.
- [111] Gurudayal *et al.*, “Atomically Altered Hematite for Highly Efficient Perovskite Tandem Water-Splitting Devices,” *ChemSusChem*, vol. 10, no. 11, pp. 2449–2456, Jun. 2017.
- [112] R. H. Gonçalves and E. R. Leite, “The colloidal nanocrystal deposition process: an advanced method to prepare high performance hematite photoanodes for water splitting,” *Energy Environ. Sci.*, vol. 7, no. 7, pp. 2250–2254, 2014.
- [113] P. Liao and E. A. Carter, “Hole transport in pure and doped hematite,” *J. Appl. Phys.*, vol. 112, no. 1, p. 013701, Jul. 2012.
- [114] E. Hussak and G. T. Prior, “On Tripuhyite, a New Antimonate of Iron, from Tripuhy, Brazil,” *Mineral. Mag. J. Mineral. Soc.*, vol. 11, no. 53, pp. 302–303, Dec. 1897.
- [115] B. Mason and C. J. Vitalian, “The mineralogy of the antimony oxides and antimonates,” *Mineral. Mag. J. Mineral. Soc.*, vol. 30, no. 221, pp. 100–112, Jun. 1953.
- [116] A. Annamalai *et al.*, “Influence of  $\text{Sb}^{5+}$  as a Double Donor on Hematite ( $\text{Fe}^{5+}$ ) Photoanodes for Surface-Enhanced Photoelectrochemical Water Oxidation,” *ACS Appl. Mater. Interfaces*, vol. 10, no. 19, pp. 16467–16473, May 2018.
- [117] F. C. de Lima *et al.*, “Unveiling the dopant segregation effect at hematite interfaces,” *Appl. Phys. Lett.*, vol. 118, no. 20, p. 201602, May 2021.
- [118] C. Li, Z. Luo, T. Wang, and J. Gong, “Surface, Bulk, and Interface: Rational Design of Hematite Architecture toward Efficient Photo-Electrochemical Water Splitting,” *Adv. Mater.*, vol. 30, no. 30, p. 1707502, Jul. 2018.

- [119] C. Li *et al.*, “Surviving High-Temperature Calcination:  $\text{ZrO}_2$ -Induced Hematite Nanotubes for Photoelectrochemical Water Oxidation,” *Angew. Chemie*, vol. 129, no. 15, pp. 4214–4219, Apr. 2017.
- [120] H. Ma, W. Chen, Q. Fan, C. Ye, M. Zheng, and J. Wang, “Regulating Sn self-doping and boosting solar water splitting performance of hematite nanorod arrays grown on fluorine-doped tin oxide via low-level Hf doping,” *J. Colloid Interface Sci.*, vol. 625, pp. 585–595, Nov. 2022.
- [121] T. Hisatomi *et al.*, “Enhancement in the Performance of Ultrathin Hematite Photoanode for Water Splitting by an Oxide Underlayer,” *Adv. Mater.*, vol. 24, no. 20, pp. 2699–2702, May 2012.
- [122] K. Itoh and J. O. Bockris, “Thin Film Photoelectrochemistry: Iron Oxide,” *J. Electrochem. Soc.*, vol. 131, no. 6, pp. 1266–1271, Jun. 1984.
- [123] F. Le Formal, M. Grätzel, and K. Sivula, “Controlling Photoactivity in Ultrathin Hematite Films for Solar Water-Splitting,” *Adv. Funct. Mater.*, vol. 20, no. 7, pp. 1099–1107, Mar. 2010.
- [124] T. Hisatomi *et al.*, “A  $\text{Ga}_2\text{O}_3$  underlayer as an isomorphic template for ultrathin hematite films toward efficient photoelectrochemical water splitting,” *Faraday Discuss.*, vol. 155, no. 0, pp. 223–232, 2012.
- [125] A. Subramanian *et al.*, “Trade-off between Zr Passivation and Sn Doping on Hematite Nanorod Photoanodes for Efficient Solar Water Oxidation: Effects of a  $\text{ZrO}_2$  Underlayer and FTO Deformation,” *ACS Appl. Mater. Interfaces*, vol. 8, no. 30, pp. 19428–19437, Aug. 2016.
- [126] M. A. Butler, “Photoelectrolysis and physical properties of the semiconducting electrode  $\text{WO}_3$ ,” *J. Appl. Phys.*, vol. 48, no. 5, pp. 1914–1920, May 1977.
- [127] F. K. Lotgering, “Topotactical reactions with ferrimagnetic oxides having hexagonal crystal structures—I,” *J. Inorg. Nucl. Chem.*, vol. 9, no. 2, pp. 113–123, Feb. 1959.
- [128] M. Cornuz, M. Grätzel, and K. Sivula, “Preferential Orientation in Hematite Films for Solar Hydrogen Production via Water Splitting,” *Chem. Vap. Depos.*, vol. 16, no. 10–12, pp. 291–295, Dec. 2010.
- [129] P. Scherrer, “Bestimmung der Größe und der inneren Struktur von Kolloidteilchen mittels Röntgenstrahlen,” *GDZ Göttingen*, pp. 98–100, 1918.
- [130] K. Sivula, “Metal Oxide Photoelectrodes for Solar Fuel Production, Surface Traps, and Catalysis,” *J. Phys. Chem. Lett.*, vol. 4, no. 10, pp. 1624–1633, May 2013.

- [131] T. Lopes, L. Andrade, F. Le Formal, M. Gratzel, K. Sivula, and A. Mendes, “Hematite photoelectrodes for water splitting: evaluation of the role of film thickness by impedance spectroscopy,” *Phys. Chem. Chem. Phys.*, vol. 16, no. 31, p. 16515, Jul. 2014.
- [132] A. Hankin, F. E. Bedoya-Lora, J. C. Alexander, A. Regoutz, and G. H. Kelsall, “Flat band potential determination: avoiding the pitfalls,” *J. Mater. Chem. A*, vol. 7, no. 45, pp. 26162–26176, 2019.
- [133] K. C. Bedin, I. Rodríguez-Gutiérrez, L. R. P. Peregrino, L. Vayssieres, and F. L. Souza, “On electron loss lowering at hematite photoelectrode interfaces,” *J. Am. Ceram. Soc.*, no. March, pp. 1–14, Apr. 2022.
- [134] J. F. McAleer and L. M. Peter, “Photocurrent spectroscopy of anodic oxide films on titanium,” *Faraday Discuss. Chem. Soc.*, vol. 70, no. Imi 130, pp. 67–80, 1980.